chemosensors

MDPI

Review

Functional 2D Nanomaterials Gas Sensor for Exhaled Breath Analysis: A Review

Yuqing Zhang [1], Yanjie Wang [1,*], Kun Zhu [1], Zhiqiang Lan [1], Jie Wang [1], Jian He [1], Xiujian Chou [2] and Yong Zhou [3,*]

[1] School of Future Science and Engineering, Soochow University, Suzhou 215222, China
[2] Science and Technology on Electronic Test and Measurement Laboratory, School of Instrument and Electronics, North University of China, Taiyuan 030051, China
[3] Key Laboratory of Optoelectronic Technology and Systems of Ministry of Education of China, Chongqing University, Chongqing 400044, China
* Correspondence: yjwang0220@suda.edu.cn (Y.W.); zhyf@cqu.edu.cn (Y.Z.)

Abstract

Exhaled breath analysis has emerged as a promising non-invasive approach for disease diagnosis, leveraging gas sensors for their high sensitivity, portability, and real-time monitoring capabilities. Two-dimensional nanomaterials, such as graphene, transition metal dichalcogenides (TMDs), MXenes, black phosphorus, and metal–organic frameworks (MOFs), exhibit exceptional gas-sensing properties due to their atomic-scale thickness, ultra-large specific surface area, and tunable electronic structures. These characteristics enable enhanced gas adsorption and room-temperature operation, making them ideal for detecting ppb-level biomarkers like acetone, ammonia, and nitric oxide in breath. However, sensors based on pristine 2D materials face challenges including slow response/recovery kinetics, poor stability, weak humidity resistance, and limited selectivity in complex breath environments. To address these limitations, functionalization strategies have been developed to engineer material properties. Key approaches include heteroatom doping to modulate electronic band structures, heterojunction construction to facilitate charge transfer and improve selectivity, and noble metal decoration for catalytic enhancement of gas adsorption. Additionally, light irradiation has been employed to regulate the carrier concentration on the surface of sensitive materials. These strategies significantly boost sensor performance, achieving ppb-level detection limits, robust humidity resistance, and rapid response. Future directions involve integrating functionalized 2D materials into wearable, multiplexed sensor arrays for simultaneous biomarker detection, coupled with machine learning for real-time diagnostic platforms.

Keywords: 2D materials; gas sensors; functionalization strategies; exhaled breath; biomarker

Received: 31 May 2026
Revised: 7 July 2026
Accepted: 10 July 2026
Published: 12 July 2026

1. Introduction

Breath analysis, as a non-invasive, painless, and easy-to-operate early diagnostic technique for physiological abnormalities, has emerged as a cutting-edge research hotspot in modern medical diagnostics [1]. Compared with conventional invasive diagnostic methods such as blood tests and tissue biopsies, breath analysis enables real-time dynamic monitoring and early warning of diseases by capturing volatile organic compounds (VOCs) and inorganic gas biomarkers in exhaled breath [2]. Clinical evidence has demonstrated that multiple exhaled biomarkers manifest a distinct severity-dependent correlation with the progression of specific diseases. Specifically, elevated acetone concentration serves as a

key diagnostic indicator of diabetic ketoacidosis [3]. Similarly, abnormal exhaled ammonia levels closely correlate with the clinical course of chronic kidney disease (CKD) [4]. Furthermore, exhaled nitric oxide (NO), a well-established biomarker of airway inflammation, directly facilitates the clinical diagnosis and assessment of asthma severity. However, the low concentrations of the aforementioned breath biomarkers typically range from parts per billion (ppb) to parts per million (ppm) levels, and the breath gases are characterized by a high-humidity environment with 95–100% RH and multi-component cross-interference, which imposes extremely stringent requirements on the sensitivity, selectivity, and moisture resistance of detection sensors [5].

Gas sensors are the core devices for achieving high-specificity and high-sensitivity detection of breath biomarkers. Among them, nanomaterial-based chemiresistive sensors represent an emerging and highly promising technical route in breath analysis due to their advantages of a simple fabrication process, high structural designability, fast response/recovery speed, low manufacturing cost, and easy integration [6]. In various gas-sensitive nanomaterials, 2D nanomaterials (including graphene and its derivatives, transition metal dichalcogenides (TMDs), MXenes, black phosphorus (BP), and metal–organic frameworks (MOFs)) exhibit superior gas-sensing performance far exceeding that of conventional bulk materials due to their unique physicochemical properties such as atomic-level ultrathin thickness, ultra-high specific surface area, finely tunable electronic band structures, and abundant surface active sites [7]. For example, graphene and its derivatives possess extremely high room-temperature carrier mobility, which can accelerate the charge transfer rate during gas-sensing reactions, thereby improving the response speed of devices [8]. In addition, MOF materials have highly ordered porous structures and customizable pore sizes, enabling highly selective adsorption and recognition of target molecules with specific sizes and chemical properties through size-sieving effects and host-guest interactions [9]. Moreover, MXenes are rich in active sites such as hydroxyl and oxygen functional groups on their surfaces, which could enhance chemical interactions with gas molecules and improve the detection sensitivity and response intensity of devices [10]. These characteristics enable 2D nanomaterial-based sensors to efficiently capture trace biomarkers in exhaled breath, providing new possibilities for the early, non-invasive, and rapid diagnosis of major diseases [11]. To date, such sensors have achieved breakthrough progress in the detection of various disease-related breath biomarkers, including acetone for diabetes screening [12], ammonia for CKD diagnosis [13], and hydrogen sulfide (H_2S) for oral disease detection [14,15].

However, the application of pristine 2D nanomaterials in complex breath environments still faces numerous challenges. Firstly, the response/recovery kinetics are sluggish, making it difficult to meet the needs of clinical real-time monitoring [16]. The core mechanism lies in the fact that breath sensors need to operate at room temperature or low temperature to avoid the decomposition of biomarkers, while the reaction activation energy between gas molecules and the material surface is limited at low temperatures, resulting in a slow adsorption process. Meanwhile, 2D materials generally have high gas adsorption energy, which makes it difficult for adsorbed molecules to desorb, further prolonging the recovery time. Furthermore, the competitive adsorption of interfering gases such as ethanol, oxygen, and water vapor in exhaled breath with target molecules seriously affects the detection accuracy. For example, graphene has similar adsorption energies for acetone and ethanol, making it difficult to effectively distinguish them in multi-component systems [17–19]. Additionally, these materials suffer from limited moisture resistance, where the high specific surface area renders them susceptible to the competitive adsorption of water molecules that block active sites and degrade sensing performance [16,20]. Furthermore, long-term environmental stability remains a critical challenge. 2D materials like MoS_2 and black

phosphorus are highly vulnerable to ambient photo-oxidation, thereby severely curtailing the operational lifespan of the resultant devices [17,21]. To address the above issues, functional modification strategies have been widely applied, which could synergistically enhance gas-sensing performance through heteroatom doping, heterostructure engineering, noble metal decoration, and light irradiation activation [16,21]. For instance, Pt-doped graphene increased the adsorption energy of acetone by approximately 16 times [22]; N-doped graphene/ZnO heterojunctions shortened the ammonia response time to 2.3 s [18]; Pd-$SnSe_2$/SnO_2 heterojunctions achieved room-temperature high-moisture-resistance NO_2 sensing [16,20]; WS_2/MoS_2 heterojunctions modified by defect engineering and single atoms broke through the selectivity bottleneck [21]. In addition, studies on the temperature-controlled surface adhesion of graphene have provided a theoretical basis for optimizing adsorption–desorption kinetics [23].

Although 2D nanomaterial-based gas sensors have made remarkable progress in the field of breath analysis, current methodologies still have critical limitations [16,21,24]. On the one hand, most functional modification strategies only optimize single performance indicators, making it difficult to simultaneously meet the comprehensive requirements of clinical diagnosis for sensitivity, selectivity, moisture resistance, and long-term stability [16,20,24]. On the other hand, the practical application of sensors is limited by multiple interferences from the complex breath matrix [19,24], and the insufficient deep integration with machine learning algorithms and multi-sensor array technologies has not yet achieved simultaneous and accurate detection of multiple disease-related biomarkers [24]. Therefore, a systematic review of the functional modification strategies for 2D nanomaterials, coupled with an in-depth analysis of their underlying gas-sensing mechanisms, is of paramount importance.

This review focuses on functional 2D nanomaterial-based gas sensors for breath analysis, organized around the following core contents (Figure 1). Firstly, the characteristics of the complex detection environment of breath analysis and the clinical diagnostic value of core volatile biomarkers are outlined. Afterwards, the gas-sensing response mechanisms and intrinsic performance limitations of typical 2D nanomaterials such as graphene, TMDs, MXenes, BP, and 2D MOFs were systematically summarized. Subsequently, the working principles, fabrication methods, and gas-sensing performance enhancement effects of key strategies, including heteroatom doping, heterostructure construction, noble metal modification, and light irradiation regulation, were elaborated in detail. Finally, we dissected the critical challenges currently confronting this field and offer perspectives on future trends, particularly the convergence of wearable multi-sensor arrays and machine learning. The comprehensive analysis would serve as a systematic theoretical blueprint and technical roadmap for engineering high-performance gas sensors tailored for clinical breath diagnostics.

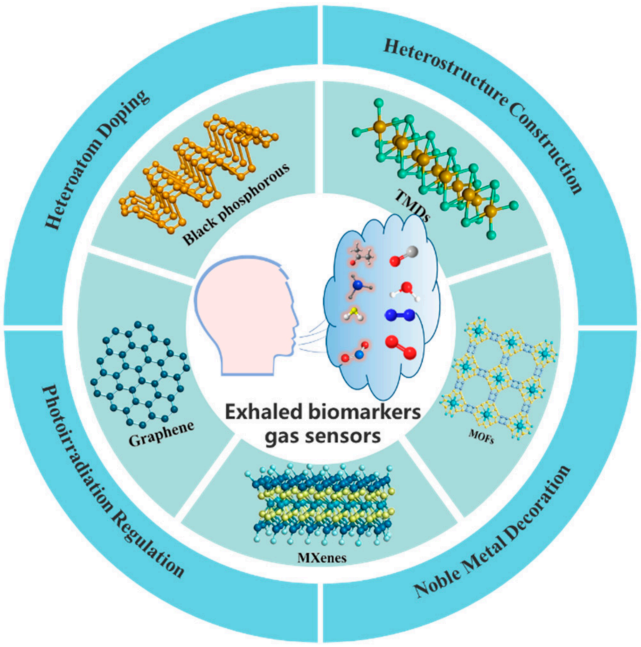

Figure 1. Schematic overview of functional 2D nanomaterial-based gas sensors for exhaled breath analysis.

2. Exhaled Breath Analysis and Gas-Sensing Fundamentals of 2D Nanomaterials

2.1. Exhaled Breath Biomarkers

Human exhaled breath consists primarily of nitrogen, oxygen, carbon dioxide, and water vapor, coexisting with hundreds of VOCs and inorganic gaseous biomarkers (e.g., NO, NH_3, H_2S). Accurate quantification and highly specific identification of disease-associated biomarkers, typically present at trace levels (ppb to ppm), establish a vital cornerstone for early non-invasive diagnostics [25–30]. The clinical correlations of key exhaled biomarkers with specific human diseases were summarized in Table 1.

As demonstrated by these clinical data, the concentration profiles of these target analytes exhibit profound dynamic variations modulated by patient demographics, disease staging, age cohorts, and environmental or physiological fluctuations. It should be noted that the clinical concentration values summarized in Table 1 represent the specific diagnostic thresholds reported in the cited literature. For instance, breath acetone, a canonical metabolic proxy for diabetes mellitus, fluctuates between 0.3 and 0.9 ppm in healthy individuals but elevates significantly above 1.8 ppm in diabetic cohorts, reaching up to 25 ppm during acute diabetic ketoacidosis (DKA) stages; furthermore, its baseline is inherently higher in older age groups and can be physiologically altered by fasting, exercise, or ketogenic diets. Similarly, fractional exhaled nitric oxide (FeNO), a key indicator of asthmatic airway inflammation, rises from a healthy baseline of 5–20 ppb to over 50 ppb during active disease stages, yet its diagnostic accuracy requires careful age-group stratification due to lower baselines in children, as well as compensation for environmental pollutants like ambient ozone. Moreover, exhaled ammonia (NH_3) traces the progression of CKD, surging from a normal range of 0.25–1.0 ppm up to 15 ppm in renal failure, though its measurement is readily confounded by oral hygiene and ambient humidity. Other trace components, such as H_2S exceeding 500 ppb in periodontal diseases and isoprene dropping below 20 ppb in lung cancer states [31,32].

Table 1. Types of exhaled biomarkers and associated diseases.

Exhaled Biomarker	Associated Disease	Clinical Concentration	References
Acetone (C_3H_6O)	Diabetes	>1.7 ppm	[33–35]
Ammonia (NH_3)	Ulcer caused by kidney disease	4.88–14.7 ppm	[36]
Ammonia (NH_3)	End-stage renal disease	>2 ppm	[37]
Hydrogen sulfide (H_2S)	Periodontitis	0.1–0.5 ppm	[14]
Hydrogen sulfide (H_2S)	Halitosis	>1 ppm	[38]
Formaldehyde (HCHO)	Lung cancer	>83 ppb	[39]
Carbon Monoxide (CO)	Helicobacter pylori infection	>6 ppm	[40]
Nitrogen oxides (NO_x)	Cardiovascular	>50 ppb	[41]
Nitric Oxide(NO)	Asthma	5–50 ppb	[42]
Ethanol(C_2H_5OH)	Fatty liver disease	>380 ppb	[43]
Methanol(CH_3OH)	Lung cancer	>216 ppb	[44]
Ketone compounds	Tumor	>100 ppb	[45]
Aliphatic compounds	COVID-19	10–250 ppb	[42]

2.2. Performance Metrics for Gas Sensors

Response is a key metric for evaluating the capability of sensors to detect trace target gases. For chemiresistive gas sensors, the sensing response (S) is widely quantified via two distinct major conventions across studies: the resistance ratio and the relative percentage resistance change [46–48]:

The first convention defines the response based on the baseline-to-exposed resistance ratio:

$$S = \frac{R_0}{R_g} \quad or \quad \frac{R_g}{R_0} \tag{1}$$

where R_0 represents the initial steady-state baseline resistance in the reference gas atmosphere, and R_g denotes the steady-state resistance upon exposure to the target gas.

The second convention evaluates the response through the relative resistance alteration, formatted as a percentage:

$$S = \frac{R_0 - R_g}{R_0} \times 100\% \quad or \quad \frac{R_g - R_0}{R_g} \times 100\% \tag{2}$$

To explicitly illustrate these definitions, consider an n-type 2D material-based sensor as an example. When exposed to reducing breath biomarker gases (e.g., acetone, ammonia, and hydrogen sulfide), the material's resistance decreases ($R_g < R_0$). Consequently, the response is calculated as $S = R_0/R_g$ according to Equation (1), or as $S = (R_0 - R_g)/R_0 \times 100\%$ according to Equation (2). Conversely, when interacting with oxidizing biomarkers (e.g., nitric oxide), the sensor resistance increases ($R_g > R_0$). In this scenario, the response is conventionally defined as $S = R_g/R_0$ for the ratio method, or $S = (R_g - R_0)/R_g \times 100\%$ for the relative change method. This dual-definition framework ensures consistent mathematical presentations across diverse literature sources compiled in this review.

Furthermore, sensor sensitivity corresponds to the response–concentration slope within the operating range, where a higher sensitivity reflects greater resistance modulation per unit concentration. This characteristic ensures discernible signals at trace levels, directly dictating the limit of detection [46–48].

Selectivity quantifies the sensor's capacity to discriminate the target analyte from competing interfering species within intricate gas matrices. Selectivity inherently arises from the intrinsic differences in adsorption energies and charge transfer efficiencies of different gas molecules on the sensing material surface. These differences can be quantita-

tively characterized via first-principles calculations, thereby guiding the rational design of highly selective active materials [49,50]. Modulation of the surface electronic structure and active site distribution of materials through strategies such as elemental doping, defect engineering, or surface functionalization can significantly enhance the specific response of sensors to target gases [25,51,52].

Humidity resistance is an indispensable performance attribute for adapting to the high-humidity environment of exhaled breath. The relative humidity of exhaled breath is typically close to 100%, and competitive adsorption of water molecules severely interferes with the detection process of target gases. The Response drift is a typical parameter for quantitatively evaluating the humidity tolerance of sensors, as shown in Equation (3):

$$Response\ drift(\%) = (S_{L\ RH} - S_{H\ RH})/S_{L\ RH} \quad (3)$$

where $S_{L\ RH}$ and $S_{H\ RH}$ represent the sensing response values under low-humidity and high-humidity conditions, respectively. A Response drift value approaching 0% indicates less interference from water molecules and superior environmental adaptability [53,54].

Kinetic performance directly determines the feasibility of real-time breath monitoring, requiring sensors to exhibit rapid response and recovery characteristics. The response time (t_{res}) is defined as the time required for the sensor resistance to reach 90% of its total change upon exposure to the target gas, while the recovery time (t_{rec}) is defined as the time needed for the resistance to return to 90% of its initial baseline after gas removal. The adsorption–desorption process of gas molecules on the surface of 2D sensing materials follows a first-order kinetic model, which can be fitted and analyzed using the following equations:

$$S(t) = S_e\left[1 - exp(-\frac{t}{\tau_{ads}})\right] \quad (4)$$

$$S(t) = S_0 exp(-\frac{t}{\tau_{des}}) \quad (5)$$

where S_e is the saturated response value, S_0 is the response value at the initial moment of desorption, and τ_{ads} and τ_{des} are the adsorption and desorption time constants, respectively [26,48,55].

To systematically evaluate the thermodynamic stability and kinetic feasibility of molecular desorption from a microscopic perspective, theoretical frameworks utilizing first-principles calculations based on density functional theory (DFT) are widely adopted. Within these paradigms, the affinity between the gas analytes and the sensitive matrix is fundamentally quantified by the adsorption energy (E_{ad}), which is defined as follows:

$$E_{ad} = E_{(layer+gas)} - E_{(layer)} - E_{(gas)} \quad (6)$$

where $E_{(layer+gas)}$, $E_{(layer)}$, and $E_{(gas)}$ represent the total ground-state energies of the host layer with the adsorbed gas molecule, the clean layer without the gas molecule, and the isolated target gas molecule, respectively. Structurally, a negative adsorption energy value ($E_{ad} < 0$) characterizes an exothermic interaction, signifying a spontaneous and stable adsorption process on the material surface [26,48,55].

According to transition state theory, the baseline recovery timescale (t_{rec}) for monolayers to desorb surface-bound molecules can be derived using the Van't Hoff–Arrhenius rate equation:

$$t_{rec} = \omega^{-1} exp(\frac{|E_{ad}|}{K_B T}) \quad (7)$$

Here, ω denotes the attempt frequency, which typically falls within the order of magnitude of 10^{-13} s^{-1}. The parameters K_B and T represent the Boltzmann's constant

and the absolute operating temperature, respectively. This mathematical relationship underscores a critical trade-off in gas sensor engineering: while a high adsorption energy ($|E_{ad}|$) is highly desirable for maximizing charge transfer and sensitivity, its exponential impact on recovery time can result in sluggish desorption kinetics or even irreversible chemisorption at room temperature, thereby directly limiting the sensor's cyclability and longevity [26,48,55].

Room-temperature operation is a crucial prerequisite for the clinical translation of breath sensors, as it effectively reduces system power consumption and prevents thermal decomposition of thermally labile biomarkers. Conventional metal oxide semiconductor sensors typically require operating temperatures of 200–400 °C, whereas 2D nanomaterials enable efficient room-temperature gas detection due to their high specific surface area, tunable bandgap, and excellent room-temperature carrier mobility [48,52,56].

The limit of detection (LoD) determines a sensor's ability to identify ultra-trace biomarkers and must meet clinical diagnostic thresholds. The LoD is determined by the intrinsic noise level and sensitivity of the sensor, and its calculation formula is as follows:

$$LoD = 3 \times \frac{\sigma}{S_{slope}} \tag{8}$$

where σ is the standard deviation of the baseline noise in the reference gas atmosphere, and S_{slope} is the slope of the calibration curve of sensing response versus gas concentration. Optimization of the intrinsic properties of sensing materials through strategies such as structural engineering, heterostructure construction, or defect regulation can effectively enhance sensitivity and reduce the LoD to ppb or even sub-ppb levels [27,57,58].

To quantitatively characterize the performance enhancement effect of different modification strategies on 2D nanomaterial-based gas sensors, the enhancement factor (E_F) is commonly introduced as a key evaluation index, which is calculated by the following formula:

$$E_F = \frac{S_F}{S_N} \tag{9}$$

where S_F denotes the response value of the modified 2D nanomaterial-based sensor to the target gas, and S_N represents the response value of the unmodified pure 2D nanomaterial-based sensor to the same concentration of the target gas under identical test conditions. This coefficient can intuitively reflect the enhancement degree of gas-sensing response achieved by modification methods. A larger E_F value indicates a more significant performance improvement effect of the corresponding modification strategy.

2.3. Gas-Sensing Mechanisms of 2D Nanomaterials

The excellent gas-sensing performance of 2D nanomaterials originates from the synergistic effect of their atomic-level thickness, ultrahigh specific surface area, and tunable electronic structure [59–61]. The gas-sensing mechanism of 2D nanomaterials primarily relies on direct charge transfer between the adsorbed gas molecules and the 2D surface [62–64], which modulates the carrier density and subsequently induces a measurable change in electrical resistance [65–67]. Transition metal dichalcogenides (TMDs), as typical 2D layered semiconductor materials, have been widely studied in the field of room-temperature gas sensing detection due to their tunable bandgap, ultra-high specific surface area, and abundant surface active sites [68–70]. Figure 2a presents the schematic of the MoS_2 gas-sensing device, showing the basic structure that enabled the detection of these charge transfer events through resistance measurements. Based on Density Functional Theory (DFT), Figure 2b displays the top views of the most energetically favorable adsorption configurations of NO_2 and NH_3 molecules on the MoS_2 surface, with calculated negative

adsorption energies of −0.14 eV and −0.16 eV, respectively, confirming the spontaneous and exothermic nature of these adsorption processes. Figure 2c schematically depicts the charge density differences upon gas adsorption, clearly demonstrating that NO_2 acted as an electron acceptor (p-type doping) while NH_3 functioned as an electron donor (n-type doping), which directly explains the opposite resistance changes observed for these two analytes. In addition, from an experimental perspective, intensive PL characterization clarified the charge transfer phenomena occurring at the MoS_2-gas interface. Specifically, NO_2 adsorption depletes electrons, enhancing the A^+ peak and suppressing the A^0 peak (Figure 2d). Whereas NH_3 adsorption accumulates electrons, leading to the suppression of the A^+ peak and enhancement of the A^0 peak (Figure 2e). These theoretical and experimental insights lay the foundation for understanding the superior sensing performance of MoS_2-based sensors, which is further enabled by the precise synthesis and structural control of high-quality atomic-layered MoS_2 materials.

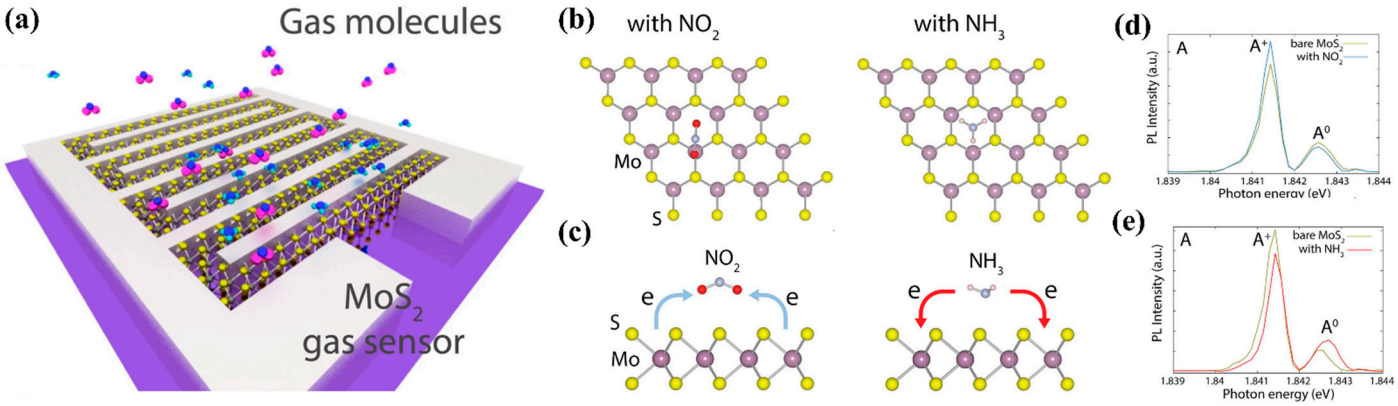

Figure 2. (**a**) Schematic of the MoS_2 gas-sensing device designed for detecting NO_2 and NH_3 gases. (**b**) Top views of the most favorable adsorption configurations of NO_2 and NH_3 molecules on the MoS_2 surface; (**c**) schematics of the charge density differences for MoS_2 in the presence of NO_2 and NH_3 gas molecules; In situ PL spectra recorded from the MoS_2 with (**d**) NO_2 and (**e**) NH_3 molecules. Reprinted with permission from Ref. [71]. Copyright © 2015, Nature Publishing Group.

2.4. Influencing Factors of Gas-Sensing Properties of 2D Nanomaterials

The gas-sensing performance of 2D nanomaterials is not determined by a single factor but is synergistically regulated by intrinsic structural characteristics and external environmental conditions. These factors ultimately determine the sensitivity, selectivity, kinetic characteristics, and long-term stability of sensors by altering the specific surface area, active site distribution, and electronic band structure of the materials [39,72,73]. Layer thickness is a core intrinsic parameter that regulates the electronic structure and gas-sensing performance of 2D nanomaterials, directly determining the bandgap width, carrier transport characteristics, and surface active site density of the materials [49,74,75]. For few-layer 2D materials, as the number of layers decreases, the quantum confinement effect gradually enhances, the bandgap increases monotonically, and the proportion of surface atoms increases significantly, providing more accessible adsorption sites for gas molecules. However, an excessively thin atomic-level structure leads to reduced mechanical strength and environmental tolerance, making it prone to oxidative degradation or structural collapse [46,51]. There is a typical optimal trade-off relationship between layer thickness and gas-sensing performance: excessively thin materials have higher specific surface area and sensitivity but suffer from severe carrier scattering and poor stability; as the number of layers increases, carrier mobility and structural stability improve, but the proportion of surface active sites decreases, leading to a decline in sensitivity. This trade-off effect originates from the dual regulation of electronic structure and surface properties by layer thickness

changes, which requires precise optimization according to the performance requirements of specific application scenarios [76,77].

In addition to the intrinsic layer thickness characteristics, the morphology structure significantly affects the response speed and sensitivity of sensors by regulating the diffusion kinetics of gas molecules and the exposure degree of active sites [58,78]. The inherent layered structure of 2D materials is prone to agglomeration, leading to the shielding of a large number of interlayer active sites, which seriously limits the exertion of their gas-sensing performance. Constructing sensing materials with specific micro–nano structures through morphology engineering can effectively solve this problem. Common optimized morphologies include porous structures, vertical array structures, and heterostructure composite structures: porous structures can construct continuous gas diffusion channels, shorten molecular diffusion paths, and increase the effective specific surface area of materials; vertical array structures can effectively inhibit the interlayer agglomeration of 2D materials, maximize the exposure of basal plane and edge active sites, and provide vertical diffusion channels for gas molecules; heterostructure composite structures can simultaneously improve the selectivity, sensitivity, and stability of materials through the interfacial synergy effect between different materials [79,80].

Defect engineering and surface functional group modification are key means to regulate the gas-sensing selectivity and adsorption strength of 2D materials [50,52]. Intrinsic defects (such as vacancies, dislocations, edge sites) and doping defects can introduce localized electronic states on the material surface, change the Fermi level position, and enhance the adsorption energy and charge transfer efficiency for specific gas molecules. For example, phosphorus vacancies can introduce dangling bonds on the surface of black phosphorus, significantly enhancing the adsorption of oxidizing gases; while heteroatom doping can precisely regulate the surface chemical properties of materials through electronic effects and geometric effects [39,72]. Surface functional group modification achieves specific recognition of target gases through hydrogen bonding, acid-base interactions, or coordination interactions, and can also improve the environmental stability of materials. By introducing specific oxygen-containing, nitrogen-containing, or fluorine-containing functional groups, specific adsorption sites can be constructed on the material surface, effectively distinguishing gas molecules with similar structures and significantly improving the selectivity of sensors [73,74].

Defect engineering, particularly the strategic introduction of point defects and atomic vacancies, serves as a powerful paradigm to fine-tune the surface reactivity and chemical selectivity of 2D nanomaterials. In pristine 2D crystal lattices, the lack of localized active sites often restricts strong gas–solid interactions; however, the creation of single-atom vacancies can profoundly disrupt the local structural symmetry and alter the intrinsic electronic properties. For instance, the departure of a lattice atom, lowering the coordination number of adjacent atoms, inevitably generates unpaired electrons, which manifest as highly reactive dangling bonds on the monolayer surface. These dangling bonds induce significant local structural deformations and sharp variations in interatomic distances, rendering the defective surface highly interactive and chemically reactive toward target gas analytes [81–83].

Mechanistically, the presence of these active vacancy sites can dramatically escalate the adsorption energies (E_{ad}), occasionally triggering a fundamental transition from weak, reversible physisorption to robust, localized chemisorption. This transition facilitates an intensive, high-quality charge transfer between the gas molecules and the 2D semiconducting matrix, directly dictating an eventual disparity in the material's electrical conductivity [81–83]. Furthermore, density of states (DOS) analyses reveal that such point defects can introduce prominent asymmetric impurity states near the Fermi level or cause

its shift toward the band edges (e.g., inducing p-type semiconducting behavior), which effectively eliminates the conventional energy band gap upon gas exposure. Consequently, tailoring the density and configuration of these atomic-scale defects allows for precise target biomarker capturing and cross-sensitivity suppression, which are vital for robust diagnostic platforms in complex exhaled breath environments.

High humidity, temperature fluctuations, and complex background gases in breath analysis scenarios can significantly interfere with the gas-sensing performance of 2D materials [46,49]. In high-humidity environments, water molecules undergo competitive adsorption on the material surface, occupying active sites and changing the surface charge distribution, leading to a decrease in the response value of target gases; temperature changes affect the adsorption–desorption kinetics of gas molecules and the carrier mobility of materials, thereby altering the response characteristics of sensors. Through surface hydrophobic modification, temperature compensation circuits, or gas filtration membranes, the interference of environmental factors can be effectively reduced. For example, fluorosilane surface modification can construct a hydrophobic layer on the material surface to inhibit the adsorption of water molecules; while temperature compensation algorithms can correct the influence of temperature changes on sensor output and improve the accuracy of detection results [51,76].

When comparing these anti-humidity strategies across various 2D materials, distinct material-specific advantages and mechanical trade-offs become evident. Surface engineering of graphene derivatives, such as reduced graphene oxide (rGO), frequently leverages structural reduction to eliminate hydrophilic oxygen groups, achieving a superhydrophobic state that effectively repels moisture. For ambient-unstable matrices like BP, covalent end-group modification via fluoroalkylsilane proves highly effective, as it simultaneously inhibits moisture adsorption and stabilizes the underlying 2D lattice. Meanwhile, physical isolation membranes (e.g., PDMS, PLA, or PTFE) deployed on graphene or MXene layers provide a robust moisture barrier without altering the material's intrinsic electronic properties, though they often introduce a trade-off in response kinetics and sensitivity due to gas diffusion limitations. Regarding long-term reliability, persistent exposure to high humidity poses severe challenges to the durability of 2D chemiresistors. Prolonged moisture exposure initiates continuous water physisorption and Grotthuss proton hopping, which dramatically decreases baseline resistance and triggers irreversible signal drift over time. Over extended operational periods, this continuous moisture accumulation can lead to structural delamination of functional coatings or irreversible lattice oxidation of the 2D channels, emphasizing that maintaining long-term baseline stability and structural integrity remains a critical bottleneck for practical breath analysis applications [84].

Despite the outstanding laboratory performance of various functional 2D nanomaterials, their successful clinical translation for non-invasive medical diagnostics, as exemplified by the real-time monitoring of diabetes mellitus via breath acetone detection, remains impeded by several systemic bottlenecks. For clinical utility in diabetes screening, gas sensors must reliably distinguish ppb levels of acetone from a complex, high-humidity volatilome containing hundreds of other interfering metabolites, which demands unparalleled cross-selectivity and baseline stability. While different 2D materials like graphene, TMDs, and MXenes offer unique electronic structures and high surface-to-volume ratios ideal for creating miniaturized point-of-care testing (POCT) arrays, they display distinct challenges in a clinical context. For instance, pristine MXenes and phosphorene are highly prone to ambient structural degradation and oxidation, which severely compromises device shelf-life and long-term diagnostic reliability, whereas graphene-based composites often require sophisticated surface functionalization or noble-metal doping to mitigate false-positive signals arising from confounding factors like dietary variations or alcohol

consumption. Ultimately, advancing from benchtop prototyping to true clinical adoption requires large-scale validation trials with diverse patient cohorts, the standardization of breath-fraction sampling protocols, and the development of scalable, highly reproducible synthesis techniques to eliminate batch-to-batch variation across sensor chips [83,85].

Comprehensively considering the core requirements of breath analysis for sensitivity, selectivity, response speed, and stability, different 2D nanomaterials exhibit differentiated performance advantages: black phosphorus-based materials have extremely high intrinsic sensitivity and adsorption energy, but their environmental stability needs to be improved; graphene and transition metal dichalcogenides have excellent electronic transport properties and fast kinetic response, suitable for real-time continuous monitoring; metal–organic framework materials show excellent molecular recognition ability and selectivity due to their controllable pore structure and abundant functional groups [58,77]. Specifically, in two-dimensional electrically conductive frameworks (2D c-MOFs), these attributes cooperatively optimize both the thermodynamic adsorption and kinetic diffusion of analytes within confined nanochannels. Beyond size-exclusive molecular sieving, this tailorable surface chemistry enables targeted host–guest interactions via open metal sites or functional ligands. Concurrently, the intrinsic in-plane $\pi - d$ conjugation or out-of-plane $\pi - \pi$ stacking provides highly efficient charge transport pathways, effectively translating these specific surface reactions into robust chemiresistive signals with significantly enhanced selectivity toward target volatile organic biomarkers [86,87].

Through multi-material composite and multi-dimensional modification strategies, the synergistic integration of the advantages of various materials can be achieved to make up for the performance shortcomings of single materials.

3. Modification Strategies of 2D Nanomaterials and Applications in Exhaled Breath Sensors

The gas-sensing performance of 2D nanomaterials is synergistically governed by the density of surface active sites, electronic band alignment, interlayer spacing, and the chemical nature of surface functional groups. Rational modification approaches encompassing heteroatom doping, heterostructure engineering, and surface functionalization represent critical pathways to optimize surface adsorption energy, charge carrier transport efficiency, catalytic reaction kinetics, and molecular recognition selectivity of the sensing materials [52,88].

3.1. Heteroatom Doping

Heteroatom doping represents a pivotal strategy for precisely tailoring the electronic configurations, surface chemical activities, and ambient stabilities of 2D nanomaterials. By embedding foreign species, such as nonmetals, transition metals, or main-group elements, into host lattices, researchers can introduce localized mid-gap defect states, modulate band structures, and increase active adsorption sites. These atomic-level alterations drastically optimize the thermodynamic binding affinities, charge-transfer efficiency, and quantum transport pathways between 2D sheets and target VOC biomarkers. Recently, extensive research has focused on functionalizing prominent 2D families, including graphyne, TMDs, MXenes, and BP, via nonmetal single doping, multi-element co-doping, and metallic substitution. These strategies provide crucial theoretical and empirical support for developing high-performance chemiresistive sensors tailored for non-invasive breath analysis.

Zhang et al. [33] systematically investigated the adsorption and transport properties of nitrogen-doped graphyne (N-GY) monolayers using DFT and NEGF methods. This study confirmed that N-GY was a direct bandgap semiconductor with a bandgap width of 0.408 eV, and all four VOC molecules were adsorbed on its surface via physisorption, with

acetone molecules exhibiting the strongest adsorption interaction (Figure 3a). Bader charge analysis revealed that all VOC molecules acted as electron acceptors, obtaining charge transfers ranging from 0.12 e to 0.20 e from N-GY.

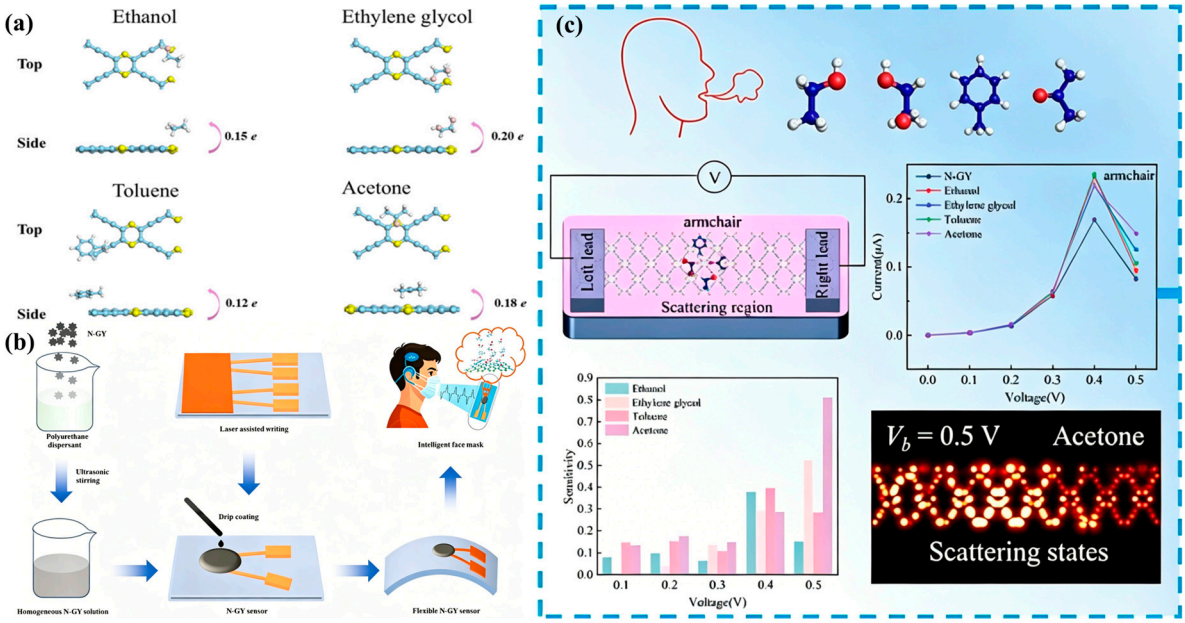

Figure 3. (**a**) Top and side views of the most stable configurations of N-GY/gas molecule systems, with the amount and direction of charge transfer between the adsorbed molecule and the surface indicated: (1) ethanol, (2) ethylene glycol, (3) toluene, (4) acetone; (**b**) schematic illustration of fabrication of the wearable flexible N-GY sensors for monitor volatile organic compounds in human breath; (**c**) schematic illustration of the application of N-GY-based sensors for the detection of volatile organic compounds in human exhaled breath and early screening of diabetes. Reproduced from Ref. [33]. Copyright © 2025, American Chemical Society.

Figure 3b shows the complete fabrication process of wearable flexible N-GY sensors and their application in an intelligent face mask for real-time monitoring of volatile organic compounds. Further transport property calculations demonstrated that under a 0.5 V bias in the armchair direction, N-GY can clearly distinguish the four gas molecules, achieving a sensitivity of up to 81% for acetone. Mechanistically, its prominent selectivity is governed by anisotropic adsorption impurity scattering that uniquely suppresses or enhances transmission coefficients within the bias energy window. Moreover, phonon spectra verified its excellent structural stability, while the physical interactions ensured ultra-fast room-temperature desorption kinetics with recovery times below the ms level, highlighting its potential as a highly reversible diagnostic layer (Figure 3c).

To address early lung cancer screening, Chen et al. [34] evaluated the sensing performance of ruthenium (Ru)-doped molybdenum disulfide (Ru-MoS_2) monolayers toward acrolein (C_3H_4O), acetone (C_3H_6O), and isoprene (C_5H_8). Ru substitution yields a robust structure with a high binding energy of −4.78 eV, while simulations confirmed its chemical and thermal stability at 500 K. Strong orbital hybridization compresses the bandgap from 1.9 eV to 0.082 eV, drastically scaling up electrical conductivity. Driven by highly active Ru 4d states, target VOCs undergo strong chemisorption (up to −3.42 eV) via covalent Ru-C/Ru-O bonds. This chemisorption-induced bandgap re-opening modulates carrier density, resulting in high resistive sensitivities of 1.09, 140.50, and 5.90, respectively, showing exceptional selectivity for C_3H_6O. Additionally, background O_2 and N_2 do not hinder detection; instead, O_2-induced n-type doping promotes the overall conductivity response.

However, the deep chemisorption wells suggest slow natural desorption kinetics, implying the necessity of thermal assistance to optimize device recovery.

To validate the sensor's performance in complex environments mimicking actual exhaled breath, the simultaneous co-adsorption of multi-component target gases alongside ambient atmospheric species was explicitly modeled. For the Ru-MoS_2 platform [34], concurrent adsorption of the ternary VOC mixture yields a robust synergistic adsorption energy of −2.11 eV, driven by an isotropic charge-transfer pathway centered at the Ru dopant site. Background interference evaluations demonstrate that while N_2 remains chemically inert, co-adsorbed O_2 induces a beneficial n-type doping effect that narrows the electronic band gap to near-zero, thereby enhancing the baseline electrical conductivity and boosting the overall sensing response. This distinct resilience to ambient gas competition firmly substantiates the theoretical feasibility of such heteroatom-doped platforms for practical, non-invasive clinical breathomics.

Aghaei et al. [35] combined a graphene-like boron-carbon-nitrogen co-doped (BC_6N) nanosheet with defect engineering to track five breath VOCs. Pristine BC_6N has a direct bandgap of 1.228 eV and exhibits weak physisorption due to localized charge polarization. Introducing a single carbon vacancy ($D_{C\text{-}N}$-BC_6N) dramatically augments surface reactivity, nearly doubling the adsorption affinities for oxygen-containing VOCs. Mechanistically, this defect triggers a semiconductor-to-metal transition via localized states on the dangling bond. NEGF transport formalisms confirmed that the sensor leverages bias-dependent quantum transport modulations rather than pure thermodynamics to achieve high selectivity. At a 1.4 V bias, it delivers an outstanding ethanol sensitivity of 61.0%, with selectivities 35.8 and 33.8 times higher than for acetone and methanol, respectively. Vacancy optimization yields highly agile desorption kinetics (4.9 s recovery for ethanol) and successfully eliminates cross-sensitivity from ambient CO_2 and H_2O, providing a compelling platform for stable and reusable breathomics.

The long-term operational viability of these heteroatom-doped configurations is fundamentally dictated by their thermodynamic and structural resilience. For instance, the structural integrity of N-GY is robustly validated by phonon spectrum evaluations and AIMD simulations. In transition-metal-doped systems, the strong anchoring of Ru dopants within the MoS_2 monolayer effectively suppresses dopant migration or aggregation. The thermodynamic and chemical durability of this Ru-MoS_2 architecture is further corroborated by high-temperature AIMD simulations and vibrational analysis confirming a complete absence of imaginary frequencies. For defect-engineered matrices like defective BC_6N nanosheets, a low vacancy formation energy substantiates excellent local structural robustness and experimental reproducibility. Furthermore, long-term sensor reliability hinges on desorptive cyclability to mitigate baseline drift; while N-GY and defective BC_6N configurations utilize weak-to-moderate physisorption to drive ultra-fast, highly reversible VOC desorption, the chemisorptive nature of Ru-MoS_2 highlights the necessity of managing baseline stability over extended sensing cycles [33–35].

Cao et al. [89] systematically investigated the adsorption behavior and gas-sensing properties of nickel (Ni)-doped molybdenum ditelluride ($MoTe_2$) monolayers toward nitrogen oxides (NO_x, x = 1, 2) via first-principles theory. Ni doping significantly enhances the surface electron density of $MoTe_2$ through strong orbital hybridization, driving a transition in the NO_x binding mechanism from weak physisorption to robust chemisorption. This chemisorption-induced electronic reconstruction narrows the material's bandgap, yielding exceptional theoretical electrical responses of −99.8% and −98.4% for NO and NO_2, respectively. Mechanistically, the sensor leverages a charge-transfer-driven resistance modulation governed by strong hybridization between Ni 3d and gas frontier orbitals. This intense chemical affinity guarantees superior selectivity over weakly interacting breath

volatiles. Furthermore, while the deep chemisorption wells ensure excellent baseline signal stability, they simultaneously pose a higher desorption barrier, implying that thermal or photo-assisted activation is essential to optimize the desorption kinetics for continuous breath monitoring.

Shi et al. [90] addressed the demand for trace methanol detection in exhaled breath by constructing a nitrogen (N)-doped clay-like $Ti_3C_2T_x$ MXene/TiO_2 spherical composite via a hydrothermal method. N doping expands the MXene interlayer spacing and introduces additional hole energy levels, creating an optimized p-n heterojunction that suppresses baseline noise. At room temperature, the sensor exhibited an ultrahigh response (R_0/R_g = 5564.65), an exceptional limit of detection (0.1194 ppm), and highly agile adsorption/desorption kinetics with response/recovery times of 14.95 s/1.49 s toward methanol. Mechanistically, in situ infrared spectroscopy and EPR verified that surface oxygen vacancies on TiO_2 act as the vital active sites for selective methanol oxidation. The spherical morphology effectively prevents nanosheet restacking to ensure excellent structural stability, while this target-specific catalytic oxidation pathway grants the composite superb selectivity against common breath interferents like ethanol and acetone.

Wang et al. [91] tackled the ambient degradation bottleneck of black phosphorus (BP) by implementing tellurium (Te) and antimony (Sb) heteroatom-engineering strategies. Doped BP nanosheets were fabricated via chemical vapor transport followed by liquid-phase exfoliation. Stability assessments demonstrated that Sb-doped BPNSs retain robust chemical stability in ambient air for over 20 days, far outperforming pristine and Te-doped counterparts. Cross-sectional HRTEM and depth XPS confirmed that heteroatom incorporation shifts the conduction band minimum of BP below the O_2/O_2^- redox potential, successfully quenching the generation of photoinduced superoxide radicals and blocking the oxidative degradation pathway. In gas-sensing trials, these stable BPNSs displayed high sensitivity and target-specific selectivity toward NO_2 and NO at room temperature. Crucially, the engineered electronic structure optimizes the binding energy with target molecules, which significantly expedites the adsorption/desorption kinetics and shortens the response/recovery times compared to intrinsic BP, providing a reliable platform for long-life BP-based breath analysis.

The operational longevity and ambient stability of these heteroatom-engineered 2D matrices are equally vital for their practical deployment. For transition-metal-doped systems such as Ni-$MoTe_2$ monolayers, structural durability is ensured by favorable binding thermodynamics that suppress dopant clustering. In hybrid architectures, like N-doped $Ti_3C_2T_x$ MXene/TiO_2 spherical composites, nitrogen incorporation coupled with heterojunction engineering significantly enhances the chemical resilience of the MXene matrix against structural degradation. Crucially, heteroatom engineering can decisively overcome the environmental vulnerability of sensitive materials; for instance, Sb-doped black phosphorus nanosheets (BPNSs) exhibit exceptional ambient stability exceeding 20 days by effectively suppressing surface oxidation dynamics and modulating the electronic band alignment [89–91].

In summary, heteroatom engineering represents a pivotal paradigm to concurrently advance the gas-sensing performance, structural durability, and ambient resilience of 2D nanomaterials by precisely tailoring their electronic profiles and surface chemistry. Although the reviewed literature underscores the success of nonmetal, transition-metal, and main-group doping across diverse platforms (graphyne, TMDs, MXenes, and BP), achieving cross-laboratory reproducibility of these functionalization protocols remains a premier hurdle for scalable manufacturing and device standardization. To successfully transition from benchtop prototypes to clinical breathomics, future research must bridge these inter-laboratory reproducibility gaps while driving innovations in atomic-precision

multi-site co-doping and synergistic heterostructure engineering, ultimately accelerating the realization of reliable, low-power platforms for early-stage disease screening.

3.2. Heterostructure Construction

Heterostructure construction represents a pivotal modification strategy that significantly elevates the sensitivity, selectivity, and response/recovery kinetics of gas sensors. By aligning multi-dimensional nanomaterials with distinct band structures, this approach leverages interfacial charge transfer, band bending, and depletion layer modulation. These configurations seamlessly integrate the advantages of individual components to deliver prominent synergistic effects, successfully overcoming the intrinsic limitations of pristine materials such as insufficient selectivity, low room-temperature activity, and sluggish kinetics [92,93]. Based on their band alignment, these architectures are classified into type I, type II, and type III heterojunctions, among which type II configurations are widely preferred in chemiresistive sensing due to their superior capability for spatial carrier separation [93]. Recently, various p-p, p-n, and n-n junctions spanning TMDs, BP, MXenes, carbon-based hybrids, and porous organic frameworks have provided a robust foundation for engineering advanced gas-sensitive materials.

Tian et al. engineered WO_3/hydroxylated hexagonal boron nitride (h-BN) Schottky heterojunctions via a template-free solvothermal method, identifying 5% weight percent as the optimal loading ratio [94]. Interfacial engineering induced preferential growth of WO_3 along the (020) crystal plane and formed strong interfacial interactions. XPS verified heterojunction formation and electron transfer, increasing oxygen vacancies to 26.3% (vs. 24.3% pristine) and introducing 6.4% surface defect oxygen. This modification effectively suppressed WO_3 nanoflake aggregation, creating abundant active sites that improved long-term structural stability. At 260 °C, the sensor exhibited an outstanding response of 390.6 to 500 ppm TEA (2.2-fold higher than pure WO_3) with a 41 ppb detection limit, 8 s response, and 60 s recovery. It maintained 99% response retention over 11 days and high tolerance to 68% RH. The accelerated adsorption/desorption kinetics and superior selectivity are driven by mesoporous pathways optimizing gas diffusion and the alignment of the Schottky barrier height (E_{h-BN} = 4.78 eV, E_{WO_3} = 4.4 eV). Upon exposure to reducing TEA, the electron depletion layer thickness is dynamically modulated, significantly enhancing sensor response.

Reddeppa et al. developed an n-type MoS_2/p-type GaN type-I p-n heterojunction via layer transfer, designing a matched band structure (1.44 eV valence and 0.67 eV conduction band offsets) and tailoring MoS_2 to two layers to balance adsorption sites and carrier transport [95]. The junction exhibited rectifying behavior, working effectively under a −2 V reverse bias. At room temperature, the sensor delivered a 47.89% response to 50 ppm NO_2, 20 and 3.2 times higher than bare GaN and pure MoS_2. Under 367 nm UV illumination, the response increased to 98.3%, response/recovery times drastically shortened to 184 s and 369 s (vs. 298 s and 1395 s in darkness), and reached 149.98% at 150 °C. The sensor showed excellent NO_2 selectivity and less than 15% degradation at 60% RH. The enhanced performance and accelerated desorption kinetics are attributed to the built-in electric field promoting charge separation. While strong chemisorption binding energy ensures outstanding selectivity, UV-induced photogenerated holes actively facilitate the rapid desorption of strongly bound gas species, dynamically modulating the heterojunction barrier height.

Han et al. innovatively constructed a $Ti_3C_2T_x$ MXene/PbS heterojunction and proposed a new mechanism for synergistic enhancement of H_2S sensing by near-infrared light activation and photothermal effect [96]. Figure 4a schematically depicts the two-step synthesis process of the MXene/PbS sensitive material via selective etching of the Ti_3AlC_2

MAX phase followed by in situ wet-chemical precipitation of PbS nanoparticles. In addition, an intelligent monitoring system integrating MXene/PbS sensors and deep learning algorithms was successfully applied to human oral health diagnosis and egg spoilage warning (Figure 4b,c), indicating the substantial development potential. Figure 4d elucidates the underlying synergistic photoactivation and photothermal sensing mechanism under 808 nm NIR light irradiation, which involves three key aspects: efficient separation of photogenerated carriers to generate abundant·O_2^- and·OH active radicals to optimize selectivity, local temperature elevation to accelerate gas adsorption/desorption kinetics, and promoted decomposition of H_2S oxidation products (S_xO_Y) for self-cleaning capability to guarantee outstanding long-term stability.

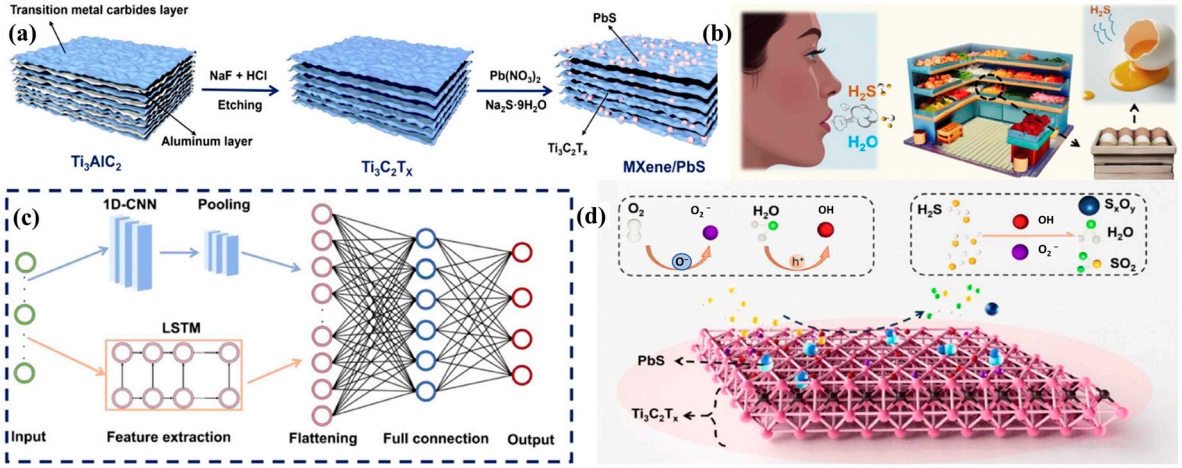

Figure 4. (**a**) Schematic illustration of the synthesis steps of MXene/PbS sensitive material; (**b**) schematic of a sensor array for exhaled gas detection and egg liquid spoilage testing; (**c**) framework diagram of the 1D-CNN/LSTM network algorithm; (**d**) schematic diagram of the H_2S sensing mechanism of MXene/PbS heterojunction. Reproduced from Ref. [96]. Copyright © 2025 Wiley-VCH GmbH.

In the field of ammonia detection, heterostructure sensors based on systems such as MXene/TMDs and BP/metal oxides have made significant progress, providing effective approaches to solve the problems of insufficient sensitivity and poor stability of single materials. Maji et al. prepared a WSe_2/V_2C MXene p-p heterostructure via electrostatic self-assembly, fabricating a room-temperature ammonia sensor on a flexible PET substrate [36]. The anchored WSe_2 nanoparticles increased the specific surface area to 16.1 m^2/g and elevated surface defects. The sensor achieved a 131% response to 2.78 ppm NH_3 at 35 °C (9.92 and 2.5 times higher than pristine WSe_2 and V_2C MXene), covering a range from 187 ppb to 23.4 ppm with a 178 ppb detection limit and 60-day stability. It maintained stable performance under a 60° bending angle and preferred polar oxygen-containing VOCs over hydrocarbons. The adsorption/desorption kinetics are driven by a 4.09 nm mesoporous structure optimizing gas transport. Furthermore, WSe_2 shields the hydrophilic terminal groups (-OH, -F) of V_2C, mitigating moisture co-adsorption to enhance stability up to 86% RH. High NH_3 selectivity is governed by its strong Lewis-base nature modulating the hole accumulation layer at the interface. Sun et al. constructed a 2D p-n heterojunction of BP nanosheet-sensitized α-MoO_3 nanoflakes via a simple physical blending method, achieving highly sensitive NH_3 detection at 40 °C [37]. The optimized sensor exhibited an excellent response of 27% to 10 ppm NH_3, a fast response/recovery speed of 275/388 s, and a low LoD of 0.4 ppm. It also showed excellent selectivity against common interfering gases such as CO_2, H_2S, and NO, while maintaining stable response performance over 22 days. Due to the hydrophilic nature of MoO_3, the sensor maintained or even slightly

improved its response in humid environments, effectively preventing moisture corrosion of the susceptible BP matrix. This humidity-tolerant performance and accelerated recovery are driven by pre-adsorbed water molecules optimizing the adsorption and diffusion of water-soluble NH_3, while the alignment of the p-n heterojunction dynamically modulates the interfacial layer thickness to boost sensitivity.

Beyond single-gas exposure studies, validating sensor performance within complex multi-component gas matrices and high-humidity backgrounds is critical to simulate true clinical exhaled breath environments. Recent advancements have addressed these cross-sensitivity challenges by evaluating 2D heterostructure performance against common breath components and interfering VOCs (CO_2, NO_2, NH_3, acetone, and ethanol) under elevated relative humidity levels of up to 86–90% [36,37,94–96]. Crucially, certain systems have transitioned from simulated matrices to actual clinical trials; for instance, a multi-channel sensor array utilizing MXene/PbS heterostructures was successfully deployed to capture and classify real human exhaled breath samples across distinct diurnal time points, achieving precise oral health diagnosis via deep-learning-assisted pattern recognition of the breath biomarkers [96].

Recently, new configurations such as carbon-based/metal oxide heterojunctions, phosphide/oxide lateral heterojunctions, and metal–organic framework (MOF)/covalent organic framework (COF) core–shell heterojunctions also exhibited remarkable gas sensing performance. Lee et al. developed a facile in situ chemical reduction route to construct SnO_2-decorated reduced graphene oxide (rGO) p-n heterojunctions for room-temperature CO_2 detection [97]. Monodisperse SnO_2 nanocrystals measuring 3 to 7 nm were uniformly anchored on wrinkled rGO nanosheets, preventing restacking and introducing abundant interfacial defects. The optimized sensor achieved a low detection limit of 5 ppm, a 1.206% response to 100 ppm CO_2, which represents a 6.7-fold enhancement over pristine rGO, and accelerated response and recovery times of 56 s and 19 s. It demonstrated excellent linearity with a correlation coefficient of 0.98002 across the 5 to 500 ppm range. This outstanding performance and fast room-temperature kinetics are driven by weak CO_2 ionization at oxygen vacancy sites to alter carrier concentration, combined with the excellent charge transport capability of rGO and band bending modulation at the p-n interfaces. Li et al. developed a novel heterostructure construction method based on in situ topological transformation of black phosphorus, successfully preparing lateral Ni_2P/NiO heteronanoplates for highly sensitive H_2S detection [98]. The optimized sensor operated at 150 °C and achieved a high response of 24.8 to 5 ppm H_2S, with response and recovery times under 10 s, an LoD of 50 ppb, and exceptional stability exceeding 5 weeks. DFT calculations revealed that the Ni_2P/NiO interface significantly increases the density of states near the Fermi level, lowering interfacial transport resistance and boosting conductivity. Moreover, the heterostructure dramatically enhanced H_2S chemisorption with a lower adsorption energy of −0.70 eV compared to individual components. This strong binding energy dictates the superior target selectivity, while the temperature-dependent surface O^- species accelerate the adsorption and desorption kinetics and guarantee excellent humidity resistance. Chen et al. constructed a core–shell structured UiO-66@TDCOF porous heterojunction, precisely regulating the energy-level structure of the MOF core through ligand engineering to realize a controllable transition from type-I to type-II band alignment. This strategy significantly enhanced visible-light-driven NO_x gas sensing at room temperature [99]. The optimal $(NH_2)_{1.24}$-UiO-66@TDCOF sensor achieved a remarkable response of 6046 to 100 ppm NO_x and an outstanding theoretical LoD of 27.8 ppb, making it highly suitable for tracking trace biomarkers in exhaled breath. The device also displayed exceptional long-term stability up to 35 days and superior selectivity against 15 common interfering gases. This performance leap stems from the robust porosity accelerating diffusion kinetics and the type-II alignment

boosting charge separation efficiency, allowing photogenerated electrons to enrich on imine bonds to provide strong reducing power toward oxidizing NO_x molecules.

To establish clinical viability for exhaled breath analysis, recent studies have rigorously validated 2D heterostructures within humid backgrounds and complex multi-component gas matrices to simulate real-world pathophysiological environments. For instance, a SnO_2-rGO hybrid sensor achieved exceptional room-temperature CO_2 detection, demonstrating strong compatibility with moisture-rich capnographic diagnostic microenvironments. To mitigate cross-sensitivity from typical respiratory co-existents, a black phosphorene-derived Ni_2P/NiO lateral heterostructure maintained a robust, high response to trace H_2S while remaining virtually insensitive to key background interferents such as NH_3 and CO. Furthermore, precise pore and interface engineering in a core–shell UiO-66@TDCOF porous heterojunction successfully isolated target NO_2 signals without baseline distortion when exposed to a synchronized multi-gas matrix containing up to 15 different interfering analytes and VOCs [97–99].

Heterostructure interface engineering profoundly optimizes 2D material chemiresistors, evolving from traditional carbon/metal oxide junctions to controllable lateral phosphide/oxide interfaces, and ultimately to precisely aligned porous MOF@COF architectures. These synergistic pathways effectively maximize electronic modulation and band matching, simultaneously elevating sensitivity, kinetics, and cross-selectivity within moisture-rich breath environments. However, viable clinical translation remains bottlenecked by cross-team reproducibility and batch-to-batch interfacial uniformity variations inherent in diverse solution-processed self-assemblies or manual layer-transfer protocols. Looking ahead, standardizing scalable, atomically precise preparation technologies, comprehensively clarifying real-world interfacial sensing mechanisms, and driving intelligent deep-learning system integration represent the primary trajectories to realize reliable, commercializable 2D heterojunction breath diagnostics.

3.3. Noble Metal Decoration

Noble metal modification is a core strategy to tailor the electronic structure, surface adsorption properties, and catalytic activity of 2D nanomaterials. Chen et al. synthesized Au nanoparticle-functionalized $Ti_3C_2T_x$ MXene hybrids through a spontaneous redox pathway, bypassing energy-intensive thermal processing [100]. Fine-tuning the precursor ratio yielded a uniform distribution of 30 nm Au crystallites, which mitigated particle aggregation and amplified accessible active sites. This chemisorption architecture manifested exceptional room-temperature capabilities, yielding a 92 ppb formaldehyde detection threshold alongside a 114% response boost relative to unmodified counterparts. The device demonstrated a profound signal-to-noise ratio of 594, exquisite selectivity for oxygenated VOCs over hydrocarbon analogs, and rigorous durability retaining minimal baseline drift (<4.3%) over five weeks. These multi-dimensional enhancements originate from Au's superb catalytic efficacy toward target dissociation and its electron-trapping proficiency, which prompts rapid charge transfer and remodels surface electronic states. DFT calculations confirmed that formaldehyde possesses a dominant binding energy of −0.728 eV, enabling accelerated adsorption kinetics and unmatched target specificity.

Rabia Gilani et al. deployed DFT simulations to systematically scrutinize Au-decorated 2D tungsten ditelluride (WTe_2) monolayers to differentiate five breath-associated VOCs from CO_2 and H_2O backgrounds [101]. Bare WTe_2 features a semiconducting profile with a 0.63 eV bandgap, wherein Au adatoms preferentially anchor at hollow topologies, ensuring magnificent thermodynamic stability via an intense binding energy of −8.61 eV. Following functionalization, profound orbital hybridization triggers a complete semiconductor-to-metal transformation. This architecture substantially upgrades analyte capture, conveying

a peak work function sensitivity of 6.69% toward HCHO driven by pronounced surface potential reconfigurations. Concurrently, temperate adsorption energies cultivate ultra-fast desorption kinetics at ambient temperature, yielding computational recovery durations from nanoseconds to milliseconds. Such swift reversibility underscores the matrix's immense promise for real-time, highly reproducible diagnostic screening.

Aref Aasi et al. integrated DFT and non-equilibrium Green's function (NEGF) methodologies to assess palladium (Pd)-modified graphene-like 2D BC_6N sheets for monitoring seven pathological breath biomarkers [41]. Unmodified BC_6N offers weak physisorption that falls short of real-world requirements. Alternatively, Pd adatoms preferentially seed onto carbon positions, catalyzing a physisorption-to-chemisorption paradigm shift that drastically reinforces the affinity parameters for NO and NO_2. The resulting Pd-BC_6N lattice retains superior structural integrity, corroborated by imaginary-frequency-free phonon spectra. Capitalizing on transport anisotropy governed by distinctive flat-band curvatures, the device delivers unparalleled directional sensitivities of 134% and 98.6% toward NO and NO_2 along the armchair orientation, coupled with exceptional selectivity matrices manifesting 12.3–74.4-fold higher responses than background distractors like CO_2 and H_2O. This diagnostic superiority arises from a chemisorption-governed semiconductor-to-metal phase change that precipitously modifies electronic conduction. Additionally, merging 498 K thermal activation with UV photostimulation effectively mitigates kinetic bottlenecks, accelerating desorption dynamics to truncate the NO_2 regeneration lifecycle to merely 270 s.

Zhang et al. deployed dispersion-corrected DFT to evaluate Ag-, Pd-, Rh-, and Ru-doped monolayer WSe_2 for selectively monitoring exhaled NO in asthmatic patients [102]. Cohesive and binding energy calculations verified superior structural stability for the Ru-doped configuration, which exhibited a dominant binding energy of −5.84 eV that securely anchors adatoms to suppress aggregation. Interface scrutiny revealed that Ru-WSe_2 undergoes strong chemisorption toward NO with an adsorption energy of −2.4 eV and a minimized bond distance of 1.84 Å, whereas CO_2 and H_2O prompt negligible charge transfer. This selective affinity stems from d-band center migration closer to the Fermi level (−1.8 eV), which amplifies molecular orbital hybridization as corroborated by a highly negative integrated crystal orbital Hamilton population of −0.84 eV. Thermodynamically, NO binding remains spontaneous below 700 K. Quantum transport and electronic state analyses indicated that only NO alters the Fermi-level density of states under multi-gas co-exposure, ensuring superb selectivity. Kinetic modeling showed that while strong chemisorption delays low-temperature desorption, operating within an optimized thermal window of 500–600 K mitigates transport bottlenecks, utilizing an ultra-low diffusion activation energy of 2.62 kJ/mol to immobilize target molecules for high-fidelity signal transduction.

While most existing experimental and theoretical studies predominantly rely on individual analyte testing or isolated humidity interference evaluations, recent first-principles advancements have contextualized sensor responses within co-existing multi-gas atmospheres. Specifically, via dispersion-corrected DFT and molecular dynamics (MD) simulations, the competitive sensing behavior of noble-metal-doped WSe_2 monolayers was investigated under simulated exhalation conditions simultaneously containing NO, CO_2, and H_2O. Thermodynamic and electronic results revealed that Ru-WSe_2 exhibits a compelling competitive adsorption advantage for the target biomarker NO with a robust adsorption energy of −2.4 eV, whereas the interactions with CO_2 and H_2O remain negligible. MD simulations verified that the strong interfacial bonding significantly suppresses the surface diffusion of NO, while H_2O molecules maintain rapid mobility due to weak affinity, and the DOS response confirmed that only NO triggers an identifiable electrical signal under such multi-gas coexistence [102].

Theoretical investigations based on first-principles calculations indicate that noble-metal decoration (e.g., on WSe_2, WTe_2, and BC_6N monolayers) yields high binding energies and stable cohesive profiles, ensuring excellent thermodynamic stability and preventing noble-metal-atom aggregation or surface diffusion. Concurrently, experimental evidence from noble-nanoparticle-decorated systems (Au-$Ti_3C_2T_x$ MXenes) demonstrates that the introduced metal nanoparticles can passivate highly reactive surface sites, thereby effectively mitigating ambient oxidation, minimizing baseline drift, and maintaining excellent functional reproducibility over extended storage or operational periods. This synergistic combination of structural integrity and chemical passivation underscores the feasibility of decorated 2D materials for durable and reliable sensing applications [41,100–102].

Chen et al. engineered Pd-Au bimetallic nanoparticle-functionalized $Ti_3C_2T_x$ MXene nanocomposites via an in situ growth strategy to construct a six-channel biomimetic sensor array integrated into a portable machine learning-assisted sensing platform [103]. The bimetallic coupling formed distinct Schottky heterojunctions that delivered electronic sensitization and catalytic synergy, effectively lowering chemical activation barriers to facilitate ultra-fast 27 s/18 s response/recovery kinetics. Relative to pristine MXene, the responsivity toward 1 ppm of diethyl ether, ethanol, acetone, and ammonia was amplified by factors of 1.73, 1.63, 2.43, and 2.73, respectively (Figure 5a,b).

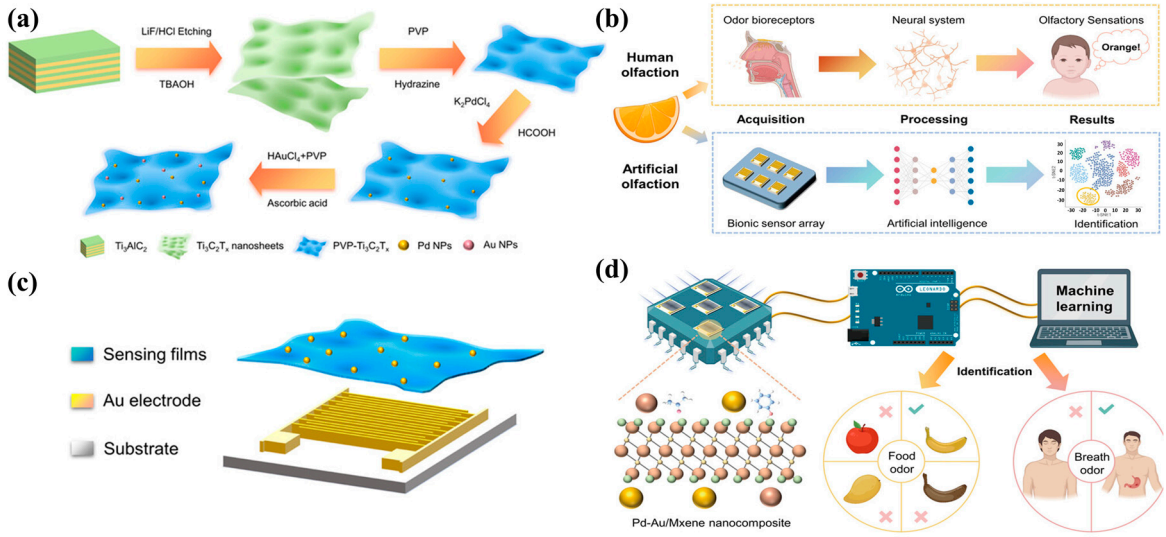

Figure 5. (**a**) Schematic illustration of the synthesis steps of Pd-Au/MXene nanocomposites via selective etching of Ti_3AlC_2 MAX phase followed by in situ growth of Pd and Au nanoparticles; (**b**) schematic illustration of artificial olfaction system; (**c**) schematic showing the components and structure of the gas sensor; (**d**) schematic of the practical constitution of IISP and its applications. Reproduced from Ref. [103]. Copyright © 2025 The Author(s). Published by Wiley-VCH GmbH.

Leveraging the distinct cross-sensitivity patterns across varying noble metal ratios, the array demonstrated exceptional matrix selectivity, successfully fingerprinting 14 distinct odor molecules (Figure 5c). When coupled with the classification and regression tree algorithm, the system yielded recognition accuracies of 89.2% for food volatile compounds and 92.0% for screening the complex breath profiles of gastric cancer patients, showcasing immense promise for stable, non-invasive point-of-care diagnostics (Figure 5d).

Cho et al. selectively anchored Au and Pt nanoparticles onto the highly reactive edge defect sites of few-layer BP via a solution-phase redox mechanism, achieving precise performance tuneability alongside a breakthrough in ambient stability [104]. The Pt-functionalized matrix exhibited unprecedented H_2 sensitivity, resolving thresholds down to 10 ppm and generating a 500% response at 1% concentration. This kinetic acceler-

ation is governed by the catalytic spillover effect, where Pt promotes rapid H_2 dissociation, lowering its work function to drive electron injection into the black phosphorus backbone and modulate hole-carrier concentration. Conversely, Au decoration induced an electronic inversion, transitioning the intrinsic p-type material into an n-type semiconductor; this inverted the sensing response toward oxidizing NO_2 from a resistance drop to a resistance increase while decreasing baseline noise 50-fold to secure a robust signal-to-noise ratio. Crucially, the noble metal clusters acted as sacrificial and physical passivation layers that effectively blocked moisture and oxygen ingress. This targeted defect passivation preserved robust gas-sensing fidelity even after 30 days of continuous atmospheric exposure, successfully resolving the long-standing degradation bottleneck of BP.

Zhao et al. constructed hierarchical 2D $CoFe_2O_4/Co_3O_4$ p-p heterojunction nanosheets using a Fe-Co MOF sacrificial template, subsequently decorating them with Pt nanoparticles to trace formaldehyde (HCHO) monitoring [105]. This ternary formulation achieved an extraordinary responsivity of 95.5 toward 100 ppm HCHO at 280 °C, which was 14.7, 6.77, and 2.9 times higher than that of single-oxide $CoFe_2O_4$, Co_3O_4, and binary $CoFe_2O_4/Co_3O_4$ systems. The detection limit reached an exceptional 6 ppb, falling well below the indoor threshold enforced by the World Health Organization. To optimize response rates, the multi-heterojunction design facilitated accelerated charge transport to expedite interfacial adsorption/desorption dynamics. Fueled by abundant reactive oxygen vacancies substantiated by EPR, the platform manifested exquisite HCHO selectivity via dipole-charge interactions, alongside strict cyclic durability that displayed a minor 3% response attenuation after 30 days. DFT and DRIFTS evaluations confirmed that this multi-dimensional improvement stems from interfacial electronic sensitization synergized with Pt catalysis, which lowers the rate-limiting oxidation pathway barrier from 1.58 eV to 1.3 eV.

Ensuring long-term operational stability and extended shelf life remains a paramount prerequisite for the practical deployment of 2D nanomaterial-based chemiresistive sensors in exhaled breath analysis. Pristine 2D matrices frequently suffer from rapid baseline drift and functional degradation due to irreversible ambient oxidation and moisture adsorption. These advancements demonstrate that noble metal decoration effectively mitigates these stability bottlenecks through surface passivation and electronic reconstruction. For instance, bimetallic co-decoration (such as Pd-Au) on MXene nanosheets forms a robust protective shield over highly reactive metallic sites, significantly suppressing atmospheric oxidation during extended ambient storage. Similarly, the dense and uniform immobilization of Au or Pt nanoparticles on few-layer BP successfully blocks the exposed surface lone-pair electrons, preventing detrimental reactions with environmental oxygen and water vapor [103–105]. This chemical passivation strategy extends reliably to MOF-derived heterostructures, where noble metal modification passivates surface coordination defects, thereby minimizing time-dependent responsiveness decay and enhancing baseline robustness under operating conditions.

Conclusively, noble metal functionalization transcends the performance limits of pristine 2D nanomaterials via synergistic electronic and chemical sensitization. Tailored surface engineering, spanning single-atom doping, nanoparticle loading, and bimetallic synergy, systematically optimizes interfacial charge transfer kinetics and environmental resilience across diverse platforms, anchoring high-performance sensing arrays for non-invasive diagnostics. Nevertheless, scalable translation demands overcoming critical bottlenecks. Beyond refining long-term operational durability and multi-component cross-selectivity, ensuring the cross-laboratory reproducibility and protocol standardization of these functionalization methods across different research groups remains a paramount challenge.

3.4. Photoirradiation Regulation

Photoirradiation represents a prevalent methodology for boosting the overall sensing capabilities of metal oxides and 2D nanomaterials. Compared to traditional thermal setups, photo-assisted stimulation adeptly circumvents the excessive power drain, abbreviated device longevity, and ignition hazards in explosive environments triggered by high-temperature operations. Jarmoshti et al. developed a silver nanoparticle-decorated reduced graphene oxide (AgNPs/rGO) nanocomposite for NH_3 gas sensing and systematically investigated the visible light modulation of its performance. By employing a blue LED emitting at 400–520 nm with an intensity of 10 mW cm^{-2}, they triggered the localized surface plasmon resonance of silver nanoparticles and spillover effects. This photoactivation enhanced the room-temperature NH_3 sensitivity by 1.7 times. Under dark conditions, the sensor achieved an intrinsic sensitivity of 5.8 at 250 ppb NH_3, a 100 ppt limit of detection, and rapid response and recovery times of 76 and 84 s, respectively. Mechanistically, the blue light interaction amplified local electric fields near the nanoparticle surfaces by 1000-fold and excited graphene electrons via the $\pi - \pi^*$ band tail. This increased gas-trapping sites and accelerated charge transfer, suppressing baseline fluctuations to deliver an excellent 95% cyclic repeatability [106].

Wang et al. engineered a visible-light-driven room-temperature HCHO sensor using a molybdenum disulfide and reduced graphene oxide hybrid (MoS_2/rGO). Under visible light above 420 nm, the heterojunction promoted surface oxygen activation and efficient charge separation. This photocatalytic mechanism converted inactive oxygen species into reactive radicals, multiplying the response to 10 ppm HCHO by 8.2 times from 8.5% to 64%, and shrinking response time from 79 to 17 s. The device achieved a 20 ppb detection limit, excellent baseline reversibility, and 90-day stability. Notably, photoactivation overcame moisture passivation, retaining a 28% response even at 80% relative humidity [107].

Pena et al. optimized multilayer graphene gas sensors through 275 nm ultraviolet photoactivation to eliminate partial recovery and baseline hysteresis. This deep ultraviolet wavelength precisely coupled with $\pi - \pi^*$ electronic transitions in the carbon lattice, generating electron–hole pairs that drove in situ photodesorption of contaminants. Continuous ultraviolet exposure accelerated the response rate by 70% and ensured complete baseline restoration, enabling a 30 ppb detection limit for NO_2. Notably, half-power irradiation achieved a peak NO_2 response enhancement of 550%, while amplifying CO and NH_3 responses by 270% and 300%, respectively. Crucially, characterization confirmed zero permanent structural damage, validating excellent device durability and cyclic reproducibility [108].

Harutyunyan et al. pioneered a continuous in situ UV photoactivation strategy to dynamically clean pristine monolayer graphene surfaces, effectively eliminating doping interferences from trace environmental contaminants to unlock its intrinsic sensitivity. This photoirradiation regulation approach enabled the sensor to achieve an ultra-low detection limit of 158 ppq for NO at room temperature, representing a 300% sensitivity enhancement over carbon nanotube-based devices. The platform also delivered exceptional detection thresholds of 2.06 ppt for NO_2 and 33.2 ppt for NH_3. Mechanistically, continuous UV exposure drove photo-induced molecular desorption, dynamically maintaining graphene near its charge-neutral point to maximize active centers. This suppressed baseline drift and accelerated desorption kinetics, reducing the NH_3 detection limit by three orders of magnitude from 83.7 ppb while ensuring excellent cyclic stability [109].

A frequent limitation among these specific photo-activated platforms, including AgNPs/rGO, MoS_2/rGO, MLG, and pristine graphene, is that their evaluation predominantly relies on single-analyte streams diluted in ambient air or inert carriers. Rather than investigating simultaneous multi-gas blending to mimic actual exhaled breath, cross-selectivity

assessments are typically conducted via separate, sequential exposures. Consequently, despite achieving exceptional sub-ppm to ppq-level LoDs under UV or visible-light modulation, further validation within realistic co-existing gaseous backgrounds is highly desirable to accurately assess competitive surface kinetics.

Wu et al. employed 254 nm UV illumination to activate a p-type $MoTe_2$ sensor, achieving specific and ultrasensitive detection of ketone molecules, including C_3H_6O and $C_5H_{10}O$. This photoirradiation induced a unique reversal in the sensing response direction exclusively for ketone molecules, enabling discriminative detection in complex gas mixtures. This UV activation strategy enhanced the C_3H_6O sensitivity by two orders of magnitude, reducing the detection limit from 23 ppm in darkness to 200 ppb. Mechanistically, UV light drove the photodesorption of pre-adsorbed O_2 and H_2O contaminants, while the modified ketones acted as hole donors that modulated the metal-semiconductor Schottky barrier width to amplify channel conductance. Notably, this continuous photoactivation overcame moisture passivation, allowing the sensor to maintain a stable, humidity-independent performance under high humidity conditions [110].

Zhang et al. engineered a (001)-faceted $TiO_2/Ti_3C_2T_x$ MXene heterostructure and demonstrated that 365 nm UV illumination significantly boosted NH_3 sensing properties through efficient photogenerated carrier separation at the Schottky junction interface.

Figure 6a,b shows the top and side views of the most stable adsorption configurations of ammonia molecules on different TiO_2 crystal plane/$Ti_3C_2O_2$ heterojunctions, which reveal the superior adsorption affinity of the (001) crystal plane via DFT calculations. The synthesis process of $TiO_2/Ti_3C_2O_2$ heterojunctions is shown in Figure 6c. Under 365 nm photoactivation, the heterostructure formed an interfacial Schottky barrier that promoted efficient photogenerated carrier separation and reduced carrier recombination. The UV-assisted sensor exhibited 34 times higher sensitivity toward 30 ppm NH_3 compared to pristine titanium carbide MXene, achieving an ultra-low detection limit of 156 ppt at room temperature. This photocatalytic mechanism effectively minimized water molecule passivation and accelerated surface reaction kinetics, delivering rapid response and recovery times of 10 s and 5 s, respectively, along with exceptional long-term stability over 150 days (Figure 6d) [111].

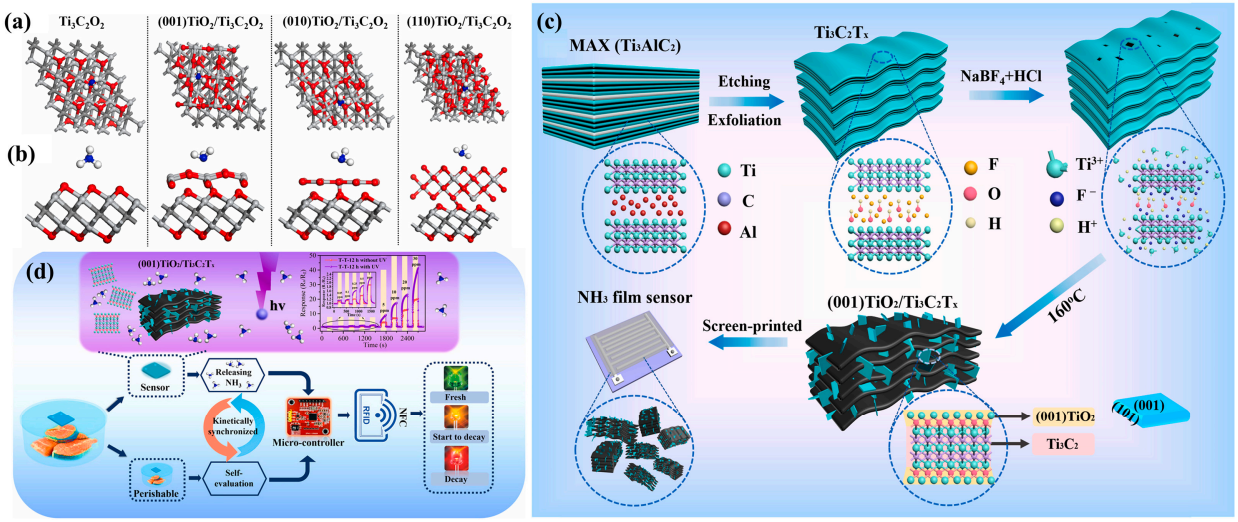

Figure 6. (**a**) Top views and (**b**) side view of the most stable adsorption configurations of ammonia gas molecules on different TiO_2 crystal plane/$Ti_3C_2O_2$ heterojunctions (silver: Ti atoms, gray: C atoms, red: O atoms, blue: N atoms, white: H atoms); (**c**) schematic illustration of the two-step synthesis process of (001) $TiO_2/Ti_3C_2T_x$ sensitive material; (**d**) schematic diagram of the overall working process of the (001)$TiO_2/Ti_3C_2T_x$-based UV-enhanced ultrasensitive ammonia sensor. Reproduced from Ref. [111]. Copyright © 2022 Elsevier B.V.

Xia et al. engineered an optoelectronic gas sensor based on sulfur-vacancy-enriched MoS2 nanosheets activated by near-infrared light above 780 nm. The sulfur vacancies introduced mid-gap localized states that effectively narrowed the band gap, enabling efficient near-infrared carrier photogeneration. Under near-infrared exposure, the pristine sensor achieved a 45% response to 200 ppb NO_2, representing an 11.5-fold enhancement compared to dark conditions. To resolve the intrinsic baseline drift stemming from carrier recombination, they decorated the sheets with zinc oxide quantum dots to construct a 2D/0D heterostructure. The resulting interfacial internal electric field promoted robust charge separation, boosting the response to 226%, lowering the detection limit to 0.1 ppb, and reducing response and recovery times to 75 and 111 s with complete reversibility. Crucially, the near-infrared-driven carriers accelerated the decomposition and desorption of chemisorbed water molecules, while the oxide layer acted as a passivation barrier against ambient oxygen degradation. This synergistic mechanism provided excellent environmental robustness, eliminating baseline hysteresis and securing reliable humidity resistance up to 80% relative humidity [112].

Photo-irradiated 2D sensing platforms have increasingly transitioned toward semi-realistic matrices to bridge the gap between controlled testing and clinical translation. Beyond idealized dry streams, configurations spanning UV-activated $MoTe_2$, (001)TiO_2/MXene, and NIR-stimulated SV-MoS_2/ZnO have successfully demonstrated robust operations under simulated breath moisture or authentic complex biogenic backgrounds. This progression reflects a pivotal shift toward evaluating competitive surface kinetics in complex ambient environments, paving the way for multi-component breath diagnostics.

Conclusively, photoactivation delivers a robust paradigm for room-temperature gas sensing, bypassing conventional thermal constraints by lowering surface activation barriers. While wavelength tailoring and architectural hybridization pave the way for IoT and personalized diagnostics, the cross-laboratory reproducibility of photoirradiation protocols remains a paramount challenge. Distinct discrepancies in illumination setups across different research groups severely hinder data standardization, particularly in power density, spot uniformity, and light source configurations. Resolving these setup-dependent inconsistencies is crucial to transition these photo-enhanced 2D platforms into reliable, industry-ready diagnostic assets.

The comprehensive sensing performance and enhancement factors of diverse functionalized 2D nanomaterial-based gas sensors are detailed in Table 2. Obviously, the functionalization strategy significantly boosts the response toward targeted clinical biomarkers. However, some sensors exhibit significant response drift under high-humidity conditions compared to dry or low-humidity environments, indicating that further refinement of the sensing layer is still required to adapt to the highly humid environment of human exhaled breath. To ensure data consistency and practical relevance, it is worth noting that all the compiled LoD parameters in Table 2 represent actual experimental detection limits directly captured under laboratory conditions, instead of theoretical estimations.

Table 2. Gas sensing performance of 2D nanomaterials-based sensors.

Method	Sensing Material	Target Gas	Response (S)	Limit of Detection (*LoD*)	Res/Rec Time (t_{res}/t_{rec})	Response Drift	E_F (S_F/S_N)	Ref.
Heteroatom Doping	Li-V_2CT_x	NH_3 (500 ppm)	3.41 [a]	——	41 s/—	——	——	[53]
	Cl-$Ti_3C_2T_x$	NH_3 (500 ppm)	13.2 [a]	——	98 s/—	——	——	[53]
	N-Graphene	NO_2 (10 ppm)	7.74% [b]	1 ppm	6.99 s/1087.09 s	——	3.15	[64]
	N-$Ti_3C_2T_x$/TiO_2	CH_3OH (100 ppm)	~652 [a]	119.4 ppb	——	7.1% (33–97% RH)	——	[90]
	Te-BP	NO (250 ppm)	~0.85 [a]	——	419 s/1625 s	——	1.06	[91]
	Sb-BP	NO (250 ppm)	~0.82 [a]	——	525 s/1540 s	——	1.03	[91]

Table 2. *Cont.*

Method	Sensing Material	Target Gas	Response (S)	Limit of Detection (*LoD*)	Res/Rec Time (t_{res}/t_{rec})	Response Drift	E_F (S_F/S_N)	Ref.
Heterostructure Construction	MoS_2/SnO_2	C_2H_5OH (200 ppm)	120% [b]	50 ppb	——	——	——	[56]
	MoS_2/ZnO	NH_3 (100 ppm)	61.92% [b]	12 ppb	——	——	——	[56]
	SnO_2/MoS_2	NH_3 (50 ppm)	90.23 [a]	——	23 s/1.6 s	——	5.36	[68]
	$SnO_2/Ti_3C_2T_x$	NH_3 (100 ppm)	10.4% [b]	25 ppb	34 s/—	35.1% (0–60% RH)	173.3	[70]
	MoS_2-GO	H_2S (100 ppm)	39.16% [b]	1 ppm	6.13 s/—	——	——	[49]
	MoS_2/SnO_2	H_2S (100 ppb)	54.4% [b]	15 ppb	90 s/581 s	——	——	[49]
	WO_3/h-BN	TEA (500 ppm)	390.6 [a]	41 ppb	8 s/60 s	62.1% (25–68% RH)	2.14	[94]
	MoS_2/GaN	NO_2 (50 ppm)	98.42% [b]	——	184 s/369 s	15% (0–60% RH)	9.6	[95]
	MoS_2/GaN	NO (50 ppm)	64.67% [b]	——	235 s/800 s	14.1% (0–40% RH)	2.32	[95]
	MXene/PbS	H_2S (10 ppm)	90% [b]	1 ppb	2 s/89 s	66.7% (30–90% RH)	4.5	[96]
	WSe_2/V_2C MXene	NH_3 (2.78 ppm)	131.8% [b]	178 ppb	118 s/97 s	27.81% (45–86% RH)	9.92	[36]
	BP/α-MoO_3	NH_3 (10 ppm)	27% [b]	0.4 ppm	275 s/388 s	27.77% (0–57.8% RH)	11.74	[37]
	SnO_2-rGO	CO_2 (100 ppm)	1.21% [b]	5 ppm	56 s/19 s	5.65% (58 ± 3% RH)	6.7	[97]
	Ni_2P/NiO	H_2S (5 ppm)	24.8 [a]	50 ppb	9.7 s/9.6 s	22.58% (50% RH)	11.27	[98]
	$(NH_2)_{1.24}$-UiO-66@TDCOF	NO_2(100 ppm)	6046 [a]	27.8 ppb	154.2 s/454.8 s	——	28.0	[99]
Noble Metal Decoration	Ag/rGO	NH_3 (0.1 ppm)	~1% [b]	1.2 ppb	5 s/6 s	——	——	[47]
	Au-$Ti_3C_2T_x$	HCHO (20 ppm)	3.0% [b]	92.2 ppb	180 s/402 s	——	2.14	[100]
	Pd-Au/$Ti_3C_2T_x$	Acetone (1 ppm)	6.84% [b]	100 ppb	——	26.6% (10–30% RH)	2.43	[103]
	Pd-Au/$Ti_3C_2T_x$	C_2H_5OH (1 ppm)	4.55% [b]	50 ppb	——	26.6% (10–30% RH)	1.63	[103]
	Pd-Au/$Ti_3C_2T_x$	NH_3(5 ppm)	——	20 ppb	27 s/18 s	26.6% (10–30% RH)	1.81	[103]
	Pt_2/$CoFe_2O_4$-Co_3O_4	HCHO (100 ppm)	95.5 [a]	6 ppb	17 s/63 s	37.2% (15–65% RH)	2.9	[105]
Photoirradiation Regulation	AgNPs/rGO	NH_3 (250 ppm)	5.8 [a]	100 ppt	76 s/84 s	—	1.7	[106]
	MoS_2/rGO	HCHO (10 ppm)	64% [b]	20 ppb	17 s/98 s	28% (80% RH)	8.2	[107]
	MLG890	NO_2 (1 ppm)	0.24 [a]	86 ppb	384 s/—	——	3.4	[108]
	MLG935	CO (1 ppm)	1.2% [b]	——	——	——	3.7	[108]
	Graphene	NO (10 ppt)	1.4% [b]	158 ppq	——	——	20	[109]
	$MoTe_2$	Acetone (100 ppm)	~57% [b]	200 ppb	180 s/180 s	~0% (45–65% RH)	38	[110]
	$TiO_2/Ti_3C_2T_x$	NH_3 (30 ppm)	40.6 [a]	156 ppt	10 s/5 s	20% (11–83% RH)	34	[111]
	MoS_2/ZnO	NO_2 (200 ppb)	226% [b]	0.1 ppb	75 s/111 s	33.6% (0–80% RH)	5.02	[112]

[a] $S = R_0/R_g$ *or* R_g/R_0, [b] $S = (R_0 - R_g)/R_0 \times 100\%$ *or* $(R_g - R_0)/R_g \times 100\%$.

4. Challenges and Perspectives

Despite the remarkable progress in two-dimensional material-based gas sensors for breath biomarker detection, the translation from laboratory prototypes to clinically deployed devices remains constrained by both commercialization bottlenecks and regulatory barriers [113–116]. Regarding commercialization, three specific gaps currently hinder the broader adoption of 2D materials. A primary challenge involves scalable synthesis and device fabrication. While CVD-grown graphene, MoS_2, or 2D COFs achieve excellent performance in controlled laboratory settings, their wafer-scale uniformity, transfer yield, and batch-to-batch reproducibility still lag behind those of established metal-oxide or

electrochemical platforms, factors that directly inflate manufacturing costs and weaken market competitiveness. Another critical issue is maintaining long-term operational stability under breath-relevant conditions. Given that exhaled breath presents a high-humidity environment, 2D sensors frequently exhibit baseline drift, reversible desorption hysteresis, or functional-group degradation, all of which must be mitigated prior to any point-of-care deployment. Furthermore, the integration of these materials raises significant form-factor and economic considerations. Developing flexible or wearable 2D sensors on polymer substrates requires low-temperature processing and robust interfacing, adding layers of process optimization that are rarely addressed in academic prototypes. From a regulatory perspective, breath-analysis sensors intended for clinical use must navigate a complex, multi-jurisdictional landscape, providing substantial clinical evidence benchmarked against gold standards such as GC–MS or SIFT-MS. Unlike blood or urine assays, breath analysis currently lacks universally adopted sampling SOPs, introducing variability that complicates validation efforts. Bridging these gaps will require closer collaboration between materials scientists, clinical validators, and regulatory consultants, positioning 2D breath sensors not merely as a sensitivity breakthrough but as a viable commercial diagnostic modality.

4.1. Key Challenges

(1) Although surface hydrophobic functionalization strategies (fluoropolymer encapsulation, self-assembled monolayer epitaxial growth, and heterojunction engineering) have significantly mitigated the direct competitive adsorption of water vapor on 2D material sensing surfaces, allowing sensors to maintain basic electrical signal outputs in high-humidity environments, the near-saturated humidity of human exhaled breath remains a formidable physical and chemical interference background. Current anti-humidity strategies typically rely on introducing hydrophobic barriers or interfacial layers, which inevitably impede the adsorption of target breath biomarkers while blocking water molecules, thereby compromising sensing sensitivity [115,117]. Furthermore, under long-term, dynamic exposure to high-humidity breath streams [118], the continuous micro-permeation of water molecules intertwines with irreversible surface passivation and non-specific adsorption of environmental background gases. This forms a complex "multi-factor coupled interference" that severely degrades the reproducibility of the sensor signals and long-term baseline stability [43,119].

(2) To modulate the surface electronic structure of 2D materials and enhance their gas-sensing activity, it is often necessary to introduce noble metal nanocluster nucleation, atomic-scale defect engineering (e.g., oxygen/sulfur vacancies), or construct hierarchical van der Waals heterojunctions [120,121]. However, current functionalization techniques predominantly rely on liquid-phase chemical exfoliation, ultrasound-assisted intercalation, or non-directional transfer processes following chemical vapor deposition (CVD) [38,65]. Atomic-scale precise control via these methods at the microscopic level still exhibits high statistical randomness, resulting in significant batch-to-batch variations in layer thickness, defect density, lateral size, and distribution of catalytic active sites across large-area fabricated functionalized 2D materials [122]. This uncontrollability of microscopic morphology and electronic structures directly translates into inconsistencies in response sensitivity, selectivity, and dynamic characteristic parameters among individual sensing units, severely hindering the industrialized, standardized integration and wafer-scale mass production of sensor arrays [65,123]. Alternatively, bottom-up direct growth configurations, particularly atomic layer deposition (ALD), have emerged as another viable preparation pathway capable of delivering high-uniformity, wafer-scale 2D film integration [123]. Nevertheless, it remains an open challenge to definitively determine which processing methodolo-

gies, whether top-down exfoliation protocols or bottom-up synthesis schemes, can be optimally scaled up and adapted for high-volume, commercially viable industrial production [122,123].

(3) Owing to their atomically thin geometry, 2D materials possess exceptionally high surface energy. While this unique physical attribute endows them with high sensitivity, it also introduces severe intrinsic chemical instability, making them highly susceptible to environmental contamination or irreversible oxidative degradation when exposed to ambient air at room temperature and atmospheric pressure. In practical clinical diagnostics or continuous breath monitoring applications, sensors must undergo dynamic adsorption–desorption physicochemical cycles [43,124]. With prolonged operational lifespans, the irreversible passivation of specific active sites on the 2D material surface, localized lattice distortions, and alterations in the Schottky barrier at the metal-electrode interface lead to severe baseline drift and sensitivity attenuation. Current end-point algorithmic compensation schemes can only mitigate data degradation at the software level; they cannot fundamentally eradicate the adverse effects arising from the intrinsic physicochemical failure of the materials [121].

To circumvent these material-level bottlenecks, recent paradigms have shifted toward alternative synthesis and atomic-level surface modification strategies to fundamentally elevate the environmental resilience of 2D platforms. On one hand, executing atomic surface engineering via ALD to conformally encapsulate reactive sites or edges with ultrathin metal oxide barriers (e.g., ZnO) has demonstrated remarkable efficacy in preventing ambient oxidation while simultaneously preserving charge transport and catalytic sensing activities [125]. On the other hand, the optimization of upstream synthetic protocols represents another robust strategy for developing 2D derivatives with intrinsic ambient stability, which natively resist oxidative degradation under atmospheric conditions. This optimization is achieved specifically through the fabrication of precursor phases with high crystallinity combined with tailored post-treatment refinement [126].

4.2. Future Outlooks

To overcome the aforementioned multi-dimensional technical bottlenecks and fully unleash the translational potential of functionalized 2D materials in precision medicine and home healthcare, future research should focus on breakthroughs in the following core directions:

(1) Future designs of sensing interfaces should transcend the traditional paradigm of static hydrophobicity that solely blocks water molecules, aiming instead to develop synergistically enhanced smart sensing interfaces capable of both extreme humidity resistance and highly efficient, specific capture of target VOC molecules [42,127]. For instance, guided by molecular dynamics simulations and first-principles density functional theory calculations, porous 2D framework materials can be engineered with precisely tailored confinement pore sizes and coexisting hydrophilic/hydrophobic micro-domains [128]. These structures can reject the permeation of water clusters via size-exclusion effects while selectively capturing ultra-trace breath biomarkers using specific high-affinity functional groups. Furthermore, the introduction of multifunctional composites with self-healing and antifouling properties will fundamentally prevent complex breath matrices from poisoning the sensing interface [129,130].

(2) Given that a single functionalized 2D material cannot achieve absolute specificity against the complex macroscopic background of exhaled breath composed of hundreds of VOCs, developing multi-channel gas sensor arrays is an inevitable path to resolve cross-sensitivity [44,131]. By cross-matching 2D materials with different functionalization mechanisms, each sensor within the array can exhibit a unique

gas-sensing profile, thereby extracting multi-dimensional breath fingerprint responses that reflect specific pathological states [131–133]. Furthermore, by leveraging deep learning algorithms, one-dimensional convolutional neural networks, and ensemble learning strategies, transient features of dynamic response curves can be comprehensively extracted to achieve deep decoupling of humidity interference, thermal drift, baseline drift, and background gases at the algorithmic level [134–136].

(3) To satisfy the stringent device consistency requirements of industrialization and portable medical electronics [40,137], there is an urgent need to develop non-destructive transfer, in situ patterned growth, and high-precision inkjet printing technologies for 2D materials to minimize randomness-induced variations at the material level [138,139]. Concurrently, dedicated efforts should be directed toward the monolithic integration of low-power 2D material sensing chips with readout integrated circuits, low-power Bluetooth transmission modules, and edge computing architectures [140,141]. By deploying lightweight machine learning models locally on the hardware, real-time in situ preprocessing of breath signals, high-order feature dimensionality reduction, and clinical early warnings can be achieved. This will enable real-time, dynamic mobile health monitoring while safeguarding patient medical data privacy [45,142].

To accelerate clinical translation, identifying the most promising 2D material systems tailored to specific target gases is paramount. For polar VOCs commonly found in breath volatilomes (e.g., acetone, ethanol), metallic MXenes (e.g., $Ti_3C_2T_x$) represent the premier platform due to their intrinsic metallic conductivity and hydrophilic surfaces, which deliver an ultrahigh signal-to-noise ratio (SNR) essential for ppb-level sensitivity [143]. Conversely, for trace inorganic gases (e.g., NO_x, NH_3), semiconducting transition metal dichalcogenides (TMDCs) and porous 2D metal oxides are highly favored, as their tunable bandgaps and high density of sub-nanometer pores maximize interfacial charge-transfer dynamics and gas adsorption sites at room temperature [137,144]. To resolve cross-sensitivity and achieve exceptional selectivity, these matrices are typically integrated into multi-channel electronic noses through bio-inspired surface engineering or multi-component 2D/2D heterojunctions to map distinct disease-specific breath fingerprints [131]. Long-term device stability is fundamentally reinforced via hybridization strategies that shield reactive edges from ambient oxidation [145], alongside advanced encapsulation or clean, polymer-assisted wet transfer approaches that successfully preserve pristine, contamination-free interfaces over centimeter scales [139]. Regarding manufacturability, recent breakthroughs have transitioned 2D fabrication from random mechanical exfoliation toward scalable micro-manufacturing, notably through high-precision inkjet printing combined with ultrafast in situ patterned growth [138], and compatibility with standardized silicon-based MEMS sensor array platforms [40,141].

Author Contributions: Conceptualization, Y.Z. (Yuqing Zhang)., and Y.W.; methodology, Y.W. and Y.Z. (Yong Zhou); software, Y.Z. (Yuqing Zhang); validation, K.Z., and Z.L.; formal analysis, J.W., and J.H.; investigation, X.C.; writing—original draft preparation, Y.Z. (Yuqing Zhang).; writing—review and editing, Y.Z. (Yuqing Zhang) and Y.W.; visualization, Y.Z. (Yuqing Zhang).; supervision, Y.Z. (Yong Zhou); project administration, Y.W. and Y.Z. (Yong Zhou); funding acquisition, Y.W. and Y.Z. (Yong Zhou). All authors have read and agreed to the published version of the manuscript.

Funding: This research was funded by the Fundamental and Frontier Research Project of Chongqing [grant number CSTB2023NSCQ-MSX0231], the China Postdoctoral Science Foundation [grant number 2025M773617], and the Jiangsu Funding Program for Excellent Postdoctoral Talent [grant number 2025ZB533].

Institutional Review Board Statement: Not applicable.

Informed Consent Statement: Not applicable.

Data Availability Statement: Not applicable.

Acknowledgments: We gratefully acknowledge Ninghua Wang (State Grid Corporation of China) and Qicheng Zhang (Soochow University, China) for their kind assistance and valuable support of this work.

Conflicts of Interest: The authors declare no conflicts of interest.

References

1. Pleil, J.D.; Stiegel, M.A.; Sobus, J.R.; Liu, Q.; Madden, M.C. Observing the Human Exposome as Reflected in Breath Biomarkers: Heat Map Data Interpretation for Environmental and Intelligence Research. *J. Breath Res.* **2011**, *5*, 037104. [CrossRef] [PubMed]
2. Konvalina, G.; Haick, H. Sensors for Breath Testing: From Nanomaterials to Comprehensive Disease Detection. *Acc. Chem. Res.* **2013**, *47*, 66–76. [CrossRef] [PubMed]
3. Novak, B.J.; Black, D.R.; Meinardi, S.; Rowland, F.S.; Pontello, A.; Cooper, D.M.; Galassetti, P.R. Exhaled Methyl Nitrate as a Noninvasive Marker of Hyperglycemia in Type 1 Diabetes. *Proc. Natl. Acad. Sci. USA* **2007**, *104*, 15613–15618. [CrossRef] [PubMed]
4. Španěl, P.; Smith, D. What is the Real Utility of Breath Ammonia Concentration Measurements in Medicine and Physiology? *J. Breath Res.* **2018**, *12*, 027102. [CrossRef] [PubMed]
5. Güntner, A.T.; Abegg, S.; Königstein, K.; Gerber, P.A.; Schmidt-Trucksäss, A.; Pratsinis, S.E. Breath Sensors for Health Monitoring. *ACS Sens.* **2019**, *4*, 268–280. [CrossRef] [PubMed]
6. Choi, S.-J.; Kim, I.-D. Recent Developments in 2D Nanomaterials for Chemiresistive-Type Gas Sensors. *Electron. Mater. Lett.* **2018**, *14*, 221–260. [CrossRef]
7. Zhang, C.-L.; Yu, S.-H. Nanoparticles Meet Electrospinning: Recent Advances and Future Prospects. *Chem. Soc. Rev.* **2014**, *43*, 4423–4448. [CrossRef] [PubMed]
8. Liu, L.; Zhang, D.; Zhang, Q.; Chen, X.; Xu, G.; Lu, Y.; Liu, Q. Smartphone-Based Sensing System Using ZnO and Graphene Modified Electrodes for VOCs Detection. *Biosens. Bioelectron.* **2017**, *93*, 94–101. [CrossRef] [PubMed]
9. Lin, Y.; Li, Y.; Cao, Y.; Wang, X. Two-Dimensional MOFs: Design & Synthesis and Applications. *Chem.–Asian J.* **2021**, *16*, 3281–3298. [CrossRef] [PubMed]
10. Xia, S.; Luo, X. Analysis of 2D Nanomaterial BC_3 for COVID-19 Biomarker Ethyl Butyrate Sensor. *J. Mater. Chem. B* **2021**, *9*, 9221–9229. [CrossRef] [PubMed]
11. Vishinkin, R.; Haick, H. Nanoscale Sensor Technologies for Disease Detection via Volatolomics. *Small* **2015**, *11*, 6142–6164. [CrossRef] [PubMed]
12. Kumail, A.; Wei, J.; Wang, C.; Hu, J.J.; Jawad Hadi, S.M.; Waleed, A.; Wang, L.; Kim, E.S.; Kim, N.Y.; Liang, J.G.; et al. Acetone Gas Sensors for Noninvasive Diabetes Diagnosis: A Comprehensive Review. *Chem. Rec.* **2025**, *25*, e202500105. [CrossRef] [PubMed]
13. Wang, C.; Cai, Y.; Zhou, W.; Chen, P.; Xu, L.; Han, T.; Hu, Y.; Xu, X.; Liu, B.; Yu, X. A Wearable Respiration Sensor for Real-Time Monitoring of Chronic Kidney Disease. *ACS Appl. Mater. Interfaces* **2022**, *14*, 12630–12639. [CrossRef] [PubMed]
14. Yan, H.; Zhou, Y.-G. Electrical Sensing of Volatile Organic Compounds in Exhaled Breath for Disease Diagnosis. *Curr. Opin. Electrochem.* **2022**, *33*, 100922. [CrossRef]
15. Mao, S.; Chang, J.; Pu, H.; Lu, G.; He, Q.; Zhang, H.; Chen, J. Two-Dimensional Nanomaterial-Based Field-Effect Transistors for Chemical and Biological Sensing. *Chem. Soc. Rev.* **2017**, *46*, 6872–6904. [CrossRef] [PubMed]
16. Kareem, M.A.; Shittu, H.A.; Aremu, A.; Bello, I.T.; Nemufulwi, M.I.; Adamu, B.I.; Dhlamini, M.S. Two-Dimensional Nanomaterials in Gas Detection: Experimental Investigations and First-Principles Perspectives. *Mater. Today Nano* **2026**, *33*, 100788. [CrossRef]
17. Joshi, M.; Ren, X.; Lin, T.; Joshi, R. Mechanistic Insights into Gas Adsorption on 2D Materials. *Small* **2024**, *21*, e2406706. [CrossRef] [PubMed]
18. Kaushal, S.; Kaur, M.; Kaur, N.; Kumari, V.; Singh, P.P. Heteroatom-Doped Graphene as Sensing Materials: A Mini Review. *RSC Adv.* **2020**, *10*, 28608–28629. [CrossRef] [PubMed]
19. Xu, Y.; Li, X.; Song, Y.; Zhang, R.; Yuan, W.; Xia, D.; Xue, Q.; Yin, F. End Group Modification for Black Phosphorus: Simultaneous Improvement of Chemical Stability and Gas Sensing Performance. *ACS Appl. Mater. Interfaces* **2021**, *13*, 50270–50280. [CrossRef] [PubMed]
20. Bag, A.; Lee, N.-E. Gas Sensing with Heterostructures Based on Two-Dimensional Nanostructured Materials: A Review. *J. Mater. Chem. C* **2019**, *7*, 13367–13383. [CrossRef]
21. Ansari, A.; Ahmed, S.; Choudhary, S.K.; Alam, M.M.; Ali, W.; Imran, M.; Ranjan, P.; Negi, D.S. Advances in 2D Materials and Hybrid Nanoarchitectures for Gas Sensing Applications. *Adv. Eng. Mater.* **2025**, *27*, e202501615. [CrossRef]

22. Island, J.O.; Steele, G.A.; Zant, H.S.J.v.d.; Castellanos-Gomez, A. Environmental Instability of Few-Layer Black Phosphorus. *2D Mater.* **2015**, *2*, 011002. [CrossRef]
23. Chen, Y.; Fan, Z.; Zhang, Z.; Niu, W.; Li, C.; Yang, N.; Chen, B.; Zhang, H. Two-Dimensional Metal Nanomaterials: Synthesis, Properties, and Applications. *Chem. Rev.* **2018**, *118*, 6409–6455. [CrossRef] [PubMed]
24. Harun-Or-Rashid, M.; Mirzaei, S.; Nasiri, N. Nanomaterial Innovations and Machine Learning in Gas Sensing Technologies for Real-Time Health Diagnostics. *ACS Sens.* **2025**, *10*, 1620–1640. [CrossRef] [PubMed]
25. Kou, L.; Frauenheim, T.; Chen, C. Phosphorene as a Superior Gas Sensor: Selective Adsorption and Distinct I–V Response. *J. Phys. Chem. Lett.* **2014**, *5*, 2675–2681. [CrossRef] [PubMed]
26. Jeon, J.; Jang, S.K.; Jeon, S.M.; Yoo, G.; Jang, Y.H.; Park, J.-H.; Lee, S. Layer-Controlled CVD Growth of Large-Area Two-Dimensional MoS_2 Films. *Nanoscale* **2015**, *7*, 1688–1695. [CrossRef] [PubMed]
27. Noh, H.J.; Pennington, D.L.; Seo, J.M.; Cline, E.; Benedetto, G.; Baek, J.B.; Hendon, C.H.; Mirica, K.A. Reversible and Ultrasensitive Detection of Nitric Oxide Using a Conductive Two-Dimensional Metal–Organic Framework. *Angew. Chem. Int. Ed.* **2024**, *64*, e202419869. [CrossRef] [PubMed]
28. Schedin, F.; Geim, A.K.; Morozov, S.V.; Hill, E.W.; Blake, P.; Katsnelson, M.I.; Novoselov, K.S. Detection of Individual Gas Molecules Adsorbed on Graphene. *Nat. Mater.* **2007**, *6*, 652–655. [CrossRef] [PubMed]
29. Novoselov, K.S.; Geim, A.K.; Morozov, S.V.; Jiang, D.; Zhang, Y.; Dubonos, S.V.; Grigorieva, I.V.; Firsov, A.A. Electric Field Effect in Atomically Thin Carbon Films. *Science* **2004**, *306*, 666–669. [CrossRef] [PubMed]
30. Li, D.; Müller, M.B.; Gilje, S.; Kaner, R.B.; Wallace, G.G. Processable Aqueous Dispersions of Graphene Nanosheets. *Nat. Nanotechnol.* **2008**, *3*, 101–105. [CrossRef] [PubMed]
31. Gupta, M.; Verma, A.; Chaudhary, P.; Yadav, B.C. MXene and Their Integrated Composite-Based Acetone Sensors for Monitoring of Diabetes. *Mater. Adv.* **2023**, *4*, 3989–4010. [CrossRef]
32. Rudie, A.; Schornack, A.M.; Wu, Q.; Zhang, Q.; Wang, D. Two-Dimensional Ti_3C_2 MXene-Based Novel Nanocomposites for Breath Sensors for Early Detection of Diabetes Mellitus. *Biosensors* **2022**, *12*, 332. [CrossRef] [PubMed]
33. Zhang, L.; He, B.; Li, Y.; Yun, J.; Yao, L.; Zhao, H.; Yan, J.; Zhao, W.; Zhang, Z. Nitrogen-Doped Graphyne as a Promising Material for Sensing Volatile Organic Compounds in Human Breath. *ACS Sens.* **2025**, *10*, 2499–2509. [CrossRef] [PubMed]
34. Chen, X.; Wan, Q. Ru-Doped MoS_2 Monolayer for Exhaled Breath Detection on Early Lung Cancer Diagnosis: A First-Principles Investigation. *ACS Omega* **2024**, *9*, 13951–13959. [CrossRef] [PubMed]
35. Aghaei, S.M.; Aasi, A.; Farhangdoust, S.; Panchapakesan, B. Graphene-Like BC_6N Nanosheets are Potential Candidates for Detection of Volatile Organic Compounds (VOCs) in Human Breath: A DFT Study. *Appl. Surf. Sci.* **2021**, *536*, 147756. [CrossRef]
36. Maji, B.; Badhulika, S. Fully Flexible WSe_2/V_2C MXene Heterostructure-Based Gas Sensor: A Detailed Sensing Analysis for ppb Level Detection of Ammonia at Room Temperature. *J. Alloys Compd.* **2025**, *1017*, 179079. [CrossRef]
37. Sun, M.; Ding, K.; Lu, Y.; She, X.; Chen, Y.; Wang, M.; Zou, C.; Liu, X.; Zhou, Y. Two-Dimensional p-n Heterojunctions of Black Phosphorus Nanosheet-Sensitized α-MoO_3 Nanoflake for Low-Temperature Chemiresistive NH_3 Recognition. *Microchem. J.* **2024**, *207*, 111911. [CrossRef]
38. Choi, S.-J.; Jang, B.-H.; Lee, S.-J.; Min, B.K.; Rothschild, A.; Kim, I.-D. Selective Detection of Acetone and Hydrogen Sulfide for the Diagnosis of Diabetes and Halitosis Using SnO_2 Nanofibers Functionalized with Reduced Graphene Oxide Nanosheets. *ACS Appl. Mater. Interfaces* **2014**, *6*, 2588–2597. [CrossRef] [PubMed]
39. Lai, C.; Luo, X. Detection of Lung Cancer Biomarkers C_3H_6O, CH_2O, and C_5H_8 through Pd-, Pt-, and Ag-Doped BC_6N Monolayers: A Density Functional Theory Study. *ACS Omega* **2025**, *10*, 51604–51619. [CrossRef] [PubMed]
40. Bag, A.; Lee, N.E. Recent Advancements in Development of Wearable Gas Sensors. *Adv. Mater. Technol.* **2021**, *6*, 2000883. [CrossRef]
41. Aasi, A.; Mehdi Aghaei, S.; Panchapakesan, B. Outstanding Performance of Transition-Metal-Decorated Single-Layer Graphene-like BC_6N Nanosheets for Disease Biomarker Detection in Human Breath. *ACS Omega* **2021**, *6*, 4696–4707. [CrossRef] [PubMed]
42. Kaloumenou, M.; Skotadis, E.; Lagopati, N.; Efstathopoulos, E.; Tsoukalas, D. Breath Analysis: A Promising Tool for Disease Diagnosis—The Role of Sensors. *Sensors* **2022**, *22*, 1238. [CrossRef] [PubMed]
43. Yuan, R.; Yang, Y.; Zou, B.; Zhang, Y. MXene-Enabled Gas Sensors for Wearable Breath Monitoring. *Chem. Eng. J.* **2025**, *510*, 161414. [CrossRef]
44. P, H.; Rangarajan, M.; Pandya, H.J. Breath VOC Analysis and Machine Learning Approaches for Disease Screening: A Review. *J. Breath Res.* **2023**, *17*, 024001. [CrossRef] [PubMed]
45. Hu, J.; Hu, N.; Pan, D.; Zhu, Y.; Jin, X.; Wu, S.; Lu, Y. Smell Cancer by Machine Learning-Assisted Peptide/MXene Bioelectronic Array. *Biosens. Bioelectron.* **2024**, *262*, 116562. [CrossRef] [PubMed]
46. Li, T.; Yin, W.; Gao, S.; Sun, Y.; Xu, P.; Wu, S.; Kong, H.; Yang, G.; Wei, G. The Combination of Two-Dimensional Nanomaterials with Metal Oxide Nanoparticles for Gas Sensors: A Review. *Nanomaterials* **2022**, *12*, 982. [CrossRef] [PubMed]
47. Wang, C.; Wang, Y.; Yang, Z.; Hu, N. Review of Recent Progress on Graphene-Based Composite Gas Sensors. *Ceram. Int.* **2021**, *47*, 16367–16384. [CrossRef]

48. Talukdar, D.; Mohanta, D.; Ahmed, G.A. Nitrogen Doped Compound Defect in Black Phosphorene for Enhanced Gas Sensing. *Surf. Interfaces* **2024**, *51*, 104699. [CrossRef]
49. Patra, C.; Guna, V.K.; Chakraborty, S.; Mondal, S.; Nandakishora, Y. Advances in 2D Transition Metal Dichalcogenide-Based Gas Sensors. *ACS Sens.* **2025**, *10*, 6347–6379. [CrossRef] [PubMed]
50. Akash, K.; Puneet, K.; Rahul, R. *2D Materials*; Springer Nature: Singapore, 2024.
51. Chen, X.; Xu, L.; Liu, L.-L.; Zhao, L.-S.; Chen, C.-P.; Zhang, Y.; Wang, X.-C. Adsorption of Formaldehyde Molecule on the Pristine andTransition Metal Doped Graphene: First-Principles Study. *Appl. Surf. Sci.* **2017**, *396*, 1020–1025. [CrossRef]
52. Zhang, D.; Pan, W.; Tang, M.; Wang, D.; Yu, S.; Mi, Q.; Pan, Q.; Hu, Y. Diversiform Gas Sensors Based on Two-Dimensional Nanomaterials. *Nano Res.* **2023**, *16*, 11959–11991. [CrossRef]
53. Xia, Q.; Fan, Y.; Li, S.; Zhou, A.; Shinde, N.; Mane, R.S. MXene-Based Chemical Gas Sensors: Recent Developments and Challenges. *Diam. Relat. Mater.* **2023**, *131*, 109557. [CrossRef] [PubMed]
54. Khort, A.; Haiduk, Y.; Taratyn, I.; Moskovskikh, D.; Podbolotov, K.; Usenka, A.; Lapchuk, N.; Pankov, V. High-Performance Selective NO_2 Gas Sensor Based on In_2O_3–Graphene–Cu Nanocomposites. *Sci. Rep.* **2023**, *13*, 7834. [CrossRef] [PubMed]
55. Sagadevan, S.; Lett, J.A.; Weldegebrieal, G.K.; ud Dowla Biswas, M.R.; Oh, W.C.; Alshahateet, S.F.; Fatimah, I.; Mohammad, F.; Al-Lohedan, H.A.; Paiman, S.; et al. Enhanced Gas Sensing and Photocatalytic Activity of Reduced Graphene Oxide Loaded TiO_2 Nanoparticles. *Chem. Phys. Lett.* **2021**, *780*, 138897. [CrossRef]
56. Lee, E.; Yoon, Y.S.; Kim, D.-J. Two-Dimensional Transition Metal Dichalcogenides and Metal Oxide Hybrids for Gas Sensing. *ACS Sens.* **2018**, *3*, 2045–2060. [CrossRef] [PubMed]
57. Hernandez, Y.; Nicolosi, V.; Lotya, M.; Blighe, F.M.; Sun, Z.; De, S.; Mcgovern, I.T.; Holland, B.; Byrne, M.; Gun'Ko, Y.K.; et al. High-Yield Production of Graphene by Liquid-Phase Exfoliation of Graphite. *Nat. Nanotechnol.* **2008**, *3*, 563–568. [CrossRef] [PubMed]
58. Yeh, C.-H. Computational Study of Janus Transition Metal Dichalcogenide Monolayers for Acetone Gas Sensing. *ACS Omega* **2020**, *5*, 31398–31406. [CrossRef] [PubMed]
59. Ko, J.-K.; Park, I.-H.; Hong, K.; Kwon, K.C. Recent Advances in Chemoresistive Gas Sensors Using Two-Dimensional Materials. *Nanomaterials* **2024**, *14*, 1397. [CrossRef] [PubMed]
60. Hu, N.; Wang, Y.; Chai, J.; Gao, R.; Yang, Z.; Kong, E.S.-W.; Zhang, Y. Gas Sensor Based on P-Phenylenediamine Reduced Graphene Oxide. *Sens. Actuators B Chem.* **2012**, *163*, 107–114. [CrossRef]
61. Stankovich, S.; Dikin, D.A.; Piner, R.D.; Kohlhaas, K.A.; Kleinhammes, A.; Jia, Y.; Wu, Y.; Nguyen, S.T.; Ruoff, R.S. Synthesis of Graphene-Based Nanosheets Via Chemical Reduction of Exfoliated Graphite Oxide. *Carbon* **2007**, *45*, 1558–1565. [CrossRef]
62. Abbas, A.N.; Liu, B.; Chen, L.; Ma, Y.; Cong, S.; Aroonyadet, N.; Köpf, M.; Nilges, T.; Zhou, C. Black Phosphorus Gas Sensors. *ACS Nano* **2015**, *9*, 5618–5624. [CrossRef] [PubMed]
63. Chen, Z.; Wang, J.; Wang, Y. Strategies for the Performance Enhancement of Graphene-Based Gas Sensors: A Review. *Talanta* **2021**, *235*, 122745. [CrossRef] [PubMed]
64. Srivastava, S.; Kashyap, P.K.; Singh, V.; Senguttuvan, T.D.; Gupta, B.K. Nitrogen Doped High Quality CVD Grown Graphene as a Fast Responding NO_2 Gas Sensor. *New J. Chem.* **2018**, *42*, 9550–9556. [CrossRef]
65. Bhardwaj, R.; Pumera, M. Surface-Engineered 2D Nanomaterials in Gas Sensors: Advancement and Challenges. *Small* **2025**, *21*, e2410360. [CrossRef] [PubMed]
66. Pawar, K.K.; Kumar, A.; Mirzaei, A.; Kumar, M.; Kim, H.W.; Kim, S.S. 2D Nanomaterials for Realization of Flexible and Wearable Gas Sensors: A Review. *Chemosphere* **2024**, *352*, 141234. [CrossRef] [PubMed]
67. Liu, X.; Ma, T.; Pinna, N.; Zhang, J. Two-Dimensional Nanostructured Materials for Gas Sensing. *Adv. Funct. Mater.* **2017**, *27*, 1702168. [CrossRef]
68. Wang, W.; Zhen, Y.; Zhang, J.; Li, Y.; Zhong, H.; Jia, Z.; Xiong, Y.; Xue, Q.; Yan, Y.; Alharbi, N.S.; et al. SnO_2 Nanoparticles-Modified 3D-Multilayer MoS_2 Nanosheets for Ammonia Gas Sensing at Room Temperature. *Sens. Actuators B Chem.* **2020**, *321*, 128471. [CrossRef]
69. He, T.; Li, Y.; Zhou, Z.; Zeng, C.; Qiao, L.; Lan, C.; Yin, Y.; Li, C.; Liu, Y. Synthesis of Large-Area Uniform MoS_2 Films by Substrate-Moving Atmospheric Pressure Chemical Vapor Deposition: From Monolayer to Multilayer. *2D Mater.* **2019**, *6*, 025030. [CrossRef]
70. Yang, E.; Park, K.H.; Oh, T.; Kim, S.J. Ultra-Dense SnO_2 QDs-Decorated MXene Nanosheets with High Water Dispersibility for Rapid NH_3 Sensing at Room Temperature. *Sens. Actuators B Chem.* **2024**, *409*, 135542. [CrossRef]
71. Cho, B.; Hahm, M.G.; Choi, M.; Yoon, J.; Kim, A.R.; Lee, Y.J.; Park, S.G.; Kwon, J.D.; Kim, C.S.; Song, M.; et al. Charge-Transfer-Based Gas Sensing Using Atomic-Layer MoS_2. *Sci. Rep.* **2015**, *5*, 8052. [CrossRef] [PubMed]
72. Xu, X.; Ma, W.; Jiang, H.; Wang, X.; Liu, W.; Wang, M.; Sun, G.; Ma, N.; Ma, S.; Wang, J.; et al. Highly Selective Triethylamine Gas Sensor Based on $ZnO/Ti_3C_2T_x$ MXene Self-Assembly Heterostructure. *Sens. Actuators B Chem.* **2025**, *422*, 136595. [CrossRef]
73. Yin, M.; Qiao, X.; Wang, L.; Miura, H.; Suzuki, K. Strain-Modulated Adsorption of Gas Molecule on Graphene: First-Principles Calculations. *Diam. Relat. Mater.* **2024**, *142*, 110822. [CrossRef]

74. Goharibajestani, Z.; Yürüm, A.; Yürüm, Y. Effect of Transition Metal Oxide Nanoparticles on Gas Adsorption Properties of Graphene Nanocomposites. *Appl. Surf. Sci.* **2019**, *475*, 1070–1076. [CrossRef]
75. Sharma, S.; Saini, R.; Gupta, G.; Late, D.J. Room-Temperature Highly Sensitive and Selective NH_3 Gas Sensor Using Vertically Aligned WS_2 Nanosheets. *Nanotechnology* **2022**, *34*, 045704. [CrossRef] [PubMed]
76. Rad, A.S. Adsorption of C_2H_2 and C_2H_4 on Pt-decorated graphene nanostructure: Ab-initio study. *Synth. Met.* **2016**, *211*, 115–120. [CrossRef]
77. Wang, Z.; Jia, Z.; Li, Q.; Zhang, X.; Sun, W.; Sun, J.; Liu, B.; Ha, B. The Enhanced NO_2 Sensing Properties of SnO_2 Nanoparticles/Reduced Graphene Oxide Composite. *J. Colloid Interface Sci.* **2019**, *537*, 228–237. [CrossRef] [PubMed]
78. Guo, L.-Y.; Zhao, J.; Guo, J.; Song, Y.; Jiang, P.; Jiang, T.; Huang, Z. Highly Sensitive Gas Sensors Based on Ag-Doped SnS Monolayer for NO_2 and NO Harmful Gases Detection. *IEEE Sens. J.* **2024**, *24*, 17418–17423. [CrossRef]
79. Lee, G.; Kim, S.; Jung, S.; Jang, S.; Kim, J. Suspended Black Phosphorus Nanosheet Gas Sensors. *Sens. Actuators B Chem.* **2017**, *250*, 569–573. [CrossRef]
80. Yang, S.; Wang, Z.; Dai, X.; Xiao, J.; Long, M.; Chen, T. First-Principles Study of Gas Molecule Adsorption on C-Doped Zigzag Phosphorene Nanoribbons. *Coatings* **2019**, *9*, 763. [CrossRef]
81. Mehdi Aghaei, S.; Aasi, A.; Panchapakesan, B. Experimental and Theoretical Advances in MXene-Based Gas Sensors. *ACS Omega* **2021**, *6*, 2450–2461. [CrossRef] [PubMed]
82. Sun, B.; Lv, H.; Liu, Z.; Wang, J.; Bai, X.; Zhang, Y.; Chen, J.; Kan, K.; Shi, K. Co_3O_4@PEI/$Ti_3C_2T_x$ MXene Nanocomposites for A Highly Sensitive NO_x Gas Sensor with A Low Detection Limit. *J. Mater. Chem. A* **2021**, *9*, 6335–6344. [CrossRef]
83. Verma, A.; Yadav, B.C. 2D/2D Nanostructured System Based on WO_3/WS_2 for Acetone Sensor and Breath Analyzer. *ACS Appl. Nano Mater.* **2023**, *6*, 5493–5507. [CrossRef]
84. Wang, Y.; Zhou, Y. Recent Progress on Anti-Humidity Strategies of Chemiresistive Gas Sensors. *Materials* **2022**, *15*, 8728. [CrossRef]
85. Li, X.; Fu, Y.; Lin, Y.; Du, D. Emerging 2D Materials and Their Hybrid Nanostructures for Label-Free Optical Biosensing: Recent Progress and Outlook. *Adv. Funct. Mater.* **2025**, *36*, e13767. [CrossRef] [PubMed]
86. Park, C.; Baek, J.W.; Shin, E.; Kim, I.-D. Two-Dimensional Electrically Conductive Metal–Organic Frameworks as Chemiresistive Sensors. *ACS Nanosci. Au* **2023**, *3*, 353–374. [CrossRef] [PubMed]
87. Naderlou, S.; Vahedpour, M.; Franz, D.M. Exploring the Role of Functional Groups in Modulating NO and CO Adsorption and Diffusion in 2D (Zn)MOF-470: A Multiscale Computational Study. *J. Phys. Chem. C* **2023**, *127*, 19301–19323. [CrossRef]
88. Sun, Y.-F.; Liu, S.-B.; Meng, F.-L.; Liu, J.-Y.; Jin, Z.; Kong, L.-T.; Liu, J.-H. Metal Oxide Nanostructures and Their Gas Sensing Properties: A Review. *Sensors* **2012**, *12*, 2610–2631. [CrossRef] [PubMed]
89. Cao, W.; Zhao, Q.; Yang, L.; Cui, H. Enhanced NOx Adsorption and Sensing Properties of $MoTe_2$ Monolayer by Ni-Doping: A First-Principles Study. *Surf. Interfaces* **2021**, *26*, 101372. [CrossRef]
90. Shi, Z.; Qiao, L.; Jia, Z.; Zhang, P.; Liu, B.; Gao, L. N-Doped Clay-Like $Ti_3C_2T_x$ MXene/TiO_2 Spherical Composites for Methanol Sensing in Exhaled Breath: A Theoretical Feasibility. *Mater. Res. Bull.* **2024**, *179*, 112915. [CrossRef]
91. Wang, Y.-L.; Wu, Y.-T.; Huang, S.-S.; Wang, I.J.; Chen, C.-H. Heteroatom-Engineered Black Phosphorus Nanosheets with Ambient Stability for Selective NO_2/NO Detection. *Nanoscale* **2026**, *18*, 7034–7044. [CrossRef] [PubMed]
92. Zhou, J.; Wang, C.; Zhang, X.; Jiang, L.; Wu, R. Advances in Two-Dimensional Layered Materials for Gas Sensing. *Mater. Sci. Eng. R Rep.* **2024**, *161*, 100872. [CrossRef]
93. Mathew, M.; Shinde, P.V.; Samal, R.; Rout, C.S. A Review on Mechanisms and Recent Developments in p-n Heterojunctions of 2D Materials for Gas Sensing Applications. *J. Mater. Sci.* **2021**, *56*, 9575–9604. [CrossRef]
94. Tian, W.; Wang, Y.; Zhang, Y.; Cao, J.; Guan, R.-F. WO_3 Nanoflakes Coupled with Hexagonal Boron Nitride Nanosheets for Triethylamine Sensing. *ACS Appl. Nano Mater.* **2021**, *4*, 6316–6327. [CrossRef]
95. Reddeppa, M.; Park, B.-G.; Murali, G.; Choi, S.H.; Chinh, N.D.; Kim, D.; Yang, W.; Kim, M.-D. NO_x Gas Sensors Based on Layer-Transferred n-MoS_2/p-GaN Heterojunction at Room Temperature: Study of UV Light Illuminations and Humidity. *Sens. Actuators B Chem.* **2020**, *308*, 127700. [CrossRef]
96. Han, Y.; Yin, Z.; Zhuang, H.; Yao, Y.; Yu, Y.; Huang, X.; Long, Z.; Zhu, Z. Synergistic Effects of Photoactivation and Photothermal in MXene Heterostructures for the Enhanced H_2S Detection Capability. *Adv. Funct. Mater.* **2025**, *35*, e09735. [CrossRef]
97. Lee, Z.Y.; Hawari, H.F.B.; Djaswadi, G.W.B.; Kamarudin, K. A Highly Sensitive Room Temperature CO_2 Gas Sensor Based on SnO_2-rGO Hybrid Composite. *Materials* **2021**, *14*, 522. [CrossRef] [PubMed]
98. He, S.; Li, L.; Liu, Y.; Su, J.; Sun, Y.; Dai, Z. A Phosphorene-Derived Ni_2P/NiO Lateral Heterostructure for Highly Sensitive and Selective H_2S Gas Detection. *Nanoscale* **2026**, *18*, 8054–8062. [CrossRef] [PubMed]
99. Chen, Y.-J.; Xu, Y.-M.; Ye, X.-L.; Luo, Z.-P.; Zhu, S.-P.; Li, K.-F.; Lu, J.-F.; Wang, G.-E.; Xu, G. Strategic Energy-Level Modulation in Porous Heterojunctions: Advancing Gas Sensing Through Type-I to Type-II Transitions. *Nat. Commun.* **2025**, *16*, 6634. [CrossRef] [PubMed]
100. Chen, W.Y.; Sullivan, C.D.; Lai, S.N.; Yen, C.C.; Jiang, X.; Peroulis, D.; Stanciu, L.A. Noble-Nanoparticle-Decorated $Ti_3C_2T_x$ MXenes for Highly Sensitive Volatile Organic Compound Detection. *ACS Omega* **2022**, *7*, 29195–29203. [CrossRef] [PubMed]

101. Gilani, R.; Alarfaji, S.S.; Nadeem, K.; Saeed, A.; Isa Khan, M. Pristine and Aurum-Decorated Tungsten Ditellurides as Sensing Materials for VOCs Detection in Exhaled Human Breath: DFT Analysis. *RSC Adv.* **2024**, *14*, 26788–26800. [CrossRef] [PubMed]
102. Zhang, S.; Tao, L.; Zhang, H.; Zhao, H.; Di, F.; Li, L.; An, B. Theoretical Study of Metal-Doped WSe_2 Sensors for NO Detection in Human Exhalation. *Surf. Interfaces* **2025**, *73*, 107553. [CrossRef]
103. Chen, Y.; Hu, J.; Hu, N.; Wu, S.; Lu, Y. Machine Learning-Assisted Pd-Au/MXene Sensor Array for Smart Gas Identification. *Small Struct.* **2025**, *6*, 2400619. [CrossRef]
104. Cho, S.-Y.; Koh, H.-J.; Yoo, H.-W.; Jung, H.-T. Tunable Chemical Sensing Performance of Black Phosphorus by Controlled Functionalization with Noble Metals. *Chem. Mater.* **2017**, *29*, 7197–7205. [CrossRef]
105. Zhao, Y.; Wang, M.; Liu, S.; Zhang, X.; Liu, G.; Qiao, G. Pt Decorated $CoFe_2O_4/Co_3O_4$ Nanosheets Derived from 2d Fe-Co Mof for Enhanced Hcho Detection. *J. Adv. Ceram.* **2025**, *14*, 9221092. [CrossRef]
106. Azizi Jarmoshti, J.; Nikfarjam, A.; Hajghassem, H.; Banihashemian, S.M. Visible Light Enhancement of Ammonia Detection Using Silver Nanoparticles Decorated on Reduced Graphene Oxide. *Mater. Res. Express* **2019**, *6*, 066306. [CrossRef]
107. Wang, J.; Deng, H.; Li, X.; Yang, C.; Xia, Y. Visible-Light Photocatalysis Enhanced Room-Temperature Formaldehyde Gas Sensing by MoS_2/rGO Hybrids. *Sens. Actuators B Chem.* **2020**, *304*, 127317. [CrossRef]
108. Peña, Á.; Matatagui, D.; Ricciardella, F.; Sacco, L.; Vollebregt, S.; Otero, D.; López-Sánchez, J.; Marín, P.; Horrillo, M.C. Optimization of Multilayer Graphene-Based Gas Sensors by Ultraviolet Photoactivation. *Appl. Surf. Sci.* **2023**, *610*, 155393. [CrossRef]
109. Chen, G.; Paronyan, T.M.; Harutyunyan, A.R. Sub-ppt Gas Detection with Pristine Graphene. *Appl. Phys. Lett.* **2012**, *101*, 053119. [CrossRef]
110. Wu, E.; Xie, Y.; Yuan, B.; Hao, D.; An, C.; Zhang, H.; Wu, S.; Hu, X.; Liu, J.; Zhang, D. Specific and Highly Sensitive Detection of Ketone Compounds Based on p-Type $MoTe_2$ under Ultraviolet Illumination. *ACS Appl. Mater. Interfaces* **2018**, *10*, 35664–35669. [CrossRef] [PubMed]
111. Zhang, D.; Yu, S.; Wang, X.; Huang, J.; Pan, W.; Zhang, J.; Meteku, B.E.; Zeng, J. UV Illumination-Enhanced Ultrasensitive Ammonia Gas Sensor Based on (001)TiO_2/MXene Heterostructure for Food Spoilage Detection. *J. Hazard. Mater.* **2022**, *423*, 127160. [CrossRef] [PubMed]
112. Xia, Y.; Hu, C.; Guo, S.; Zhang, L.; Wang, M.; Peng, J.; Xu, L.; Wang, J. Sulfur-Vacancy-Enriched MoS_2 Nanosheets Based Heterostructures for Near-Infrared Optoelectronic NO_2 Sensing. *ACS Appl. Nano Mater.* **2019**, *3*, 665–673. [CrossRef]
113. Nasiri, N.; Clarke, C. Nanostructured Gas Sensors for Medical and Health Applications: Low to High Dimensional Materials. *Biosensors* **2019**, *9*, 43. [CrossRef] [PubMed]
114. Dixit, K.; Fardindoost, S.; Ravishankara, A.; Tasnim, N.; Hoorfar, M. Exhaled Breath Analysis for Diabetes Diagnosis and Monitoring: Relevance, Challenges and Possibilities. *Biosensors* **2021**, *11*, 476. [CrossRef] [PubMed]
115. Chen, H.; Chen, J.; Liu, Y.; Li, B.; Li, H.; Zhang, X.; Lv, C.; Dong, H. Wearable Dual-Signal NH_3 Sensor with High Sensitivity for Non-invasive Diagnosis of Chronic Kidney Disease. *Langmuir* **2023**, *39*, 3420–3430. [CrossRef] [PubMed]
116. Wang, Y.; Yao, X. Application of Electrochemical Sensors Based on Nanomaterials in the Detection of Ventilator Associated Pneumonia: Clinical Effectiveness of Nursing Management. *Microchem. J.* **2025**, *218*, 115735. [CrossRef]
117. Du, B.; Kang, W.; He, Y.; Wang, Y.; Yang, X.; Meng, G.; Zhu, Z.; Lin, X.; Tan, Y.; Liang, C.; et al. Topological Insulator Bi_2Se_3 for Highly Sensitive, Selective and Anti-Humidity Gas Sensors. *iScience* **2023**, *26*, 106387. [CrossRef] [PubMed]
118. Yang, L.; Zheng, G.; Cao, Y.; Meng, C.; Li, Y.; Ji, H.; Chen, X.; Niu, G.; Yan, J.; Xue, Y.; et al. Moisture-Resistant, Stretchable NO_x Gas Sensors Based on Laser-Induced Graphene for Environmental Monitoring and Breath Analysis. *Microsyst. Nanoeng.* **2022**, *8*, 78. [CrossRef] [PubMed]
119. Robbiani, S.; Lotesoriere, B.J.; Dellacà, R.L.; Capelli, L. Physical Confounding Factors Affecting Gas Sensors Response: A Review on Effects and Compensation Strategies for Electronic Nose Applications. *Chemosensors* **2023**, *11*, 514. [CrossRef]
120. He, Q.; Zeng, Z.; Yin, Z.; Li, H.; Wu, S.; Huang, X.; Zhang, H. Fabrication of Flexible MoS_2 Thin-Film Transistor Arrays for Practical Gas-Sensing Applications. *Small* **2012**, *8*, 2994–2999. [CrossRef] [PubMed]
121. Xie, Y.; Zhang, Z.; Meng, F.; Huo, S.; Hu, X.; Niu, P.; Wu, E. Strategies and Challenges for Improving the Performance of Two-Dimensional Materials-Based Gas Sensors. *Adv. Phys. X* **2023**, *9*, 2288353. [CrossRef]
122. Zheng, W.; Lee, L.Y.S. Beyond Sonication: Advanced Exfoliation Methods for Scalable Production of 2D Materials. *Matter* **2022**, *5*, 515–545. [CrossRef]
123. Steeneken, P.G.; Soikkeli, M.; Arpiainen, S.; Rantala, A.; Jaaniso, R.; Pezone, R.; Vollebregt, S.; Lukas, S.; Kataria, S.; Houmes, M.J.A.; et al. Towards Wafer-Scale 2D Material Sensors. *2D Mater.* **2025**, *12*, 023002. [CrossRef]
124. Donarelli, M.; Ottaviano, L. 2D Materials for Gas Sensing Applications: A Review on Graphene Oxide, MoS_2, WS_2 and Phosphorene. *Sensors* **2018**, *18*, 3638. [CrossRef] [PubMed]
125. Yang, X.; Chang, X.; Liu, X.; Zheng, W.; Zhang, J. Atomic Surface Engineering of MXene for Stable Hydrogen Sensing at Low Temperature. *Small* **2025**, *21*, e10304. [CrossRef] [PubMed]

126. Li, X.; Ma, X.; Zhang, H.; Xue, N.; Yao, Q.; He, T.; Qu, Y.; Zhang, J.; Tao, X. Ambient-Stable MXene with Superior Performance Suitable for Widespread Applications. *Chem. Eng. J.* **2023**, *455*, 140635. [CrossRef]
127. Li, D.; Wang, W.; Duan, Q.; Wang, Y.; Wang, H.; He, X.; Wang, G.; Wang, W.; Li, H.; Han, D.; et al. Ensemble-Learning-Assisted Exhaled Gas Disease Analysis Based on In-Situ Construction of MOF-Derived MO_x/GaN Heterojunction Sensor Arrays. *Microsyst. Nanoeng.* **2026**, *12*, 39. [CrossRef] [PubMed]
128. Zeng, H.; Geng, X.; Zhang, S.; Zhou, B.; Liu, S.; Yang, Z. High-Throughput Computational Screening of Two-Dimensional Covalent Organic Frameworks (2D COFs) for Capturing Radon in Moist Air. *Nanomaterials* **2023**, *13*, 1532. [CrossRef] [PubMed]
129. Grunenberg, L.; Kessler, C.; Teh, T.W.; Schuldt, R.; Heck, F.; Kastner, J.; Gross, J.; Hansen, N.; Lotsch, B.V. Probing Self-Diffusion of Guest Molecules in a Covalent Organic Framework: Simulation and Experiment. *ACS Nano* **2024**, *18*, 16091–16100. [CrossRef] [PubMed]
130. Du, L.; Wang, X.; Sun, M.; Lu, Q.; Wang, Y.; Zhang, J.; Yin, G.; Lu, S. Polyurethane Nonwovens Integrated with Nanocomposite as Twist-Assisted Healing Flexible Sensor for Ultrasensitive Room-Temperature NO_2 Detection. *Adv. Mater.* **2025**, *38*, e09512. [CrossRef] [PubMed]
131. Liu, S.; Hu, N.; Hu, J.; Li, W.; Wu, S.; Ma, X.; Huo, Y.-X.; Lu, Y. DNA-Mediated Bioinspired MXene Gas Sensor Array with Machine Learning for Noninvasive Cancer Recognition. *ACS Nano* **2025**, *19*, 25363–25384. [CrossRef] [PubMed]
132. Li, Z.; Liu, Q.; Wang, Y.; Wu, L.; Jiang, X. Light-Active Anisotropic 2D MOF Heterojunctions for Fingerprint-Like Sensing of VOCs. *Anal. Chem.* **2026**, *98*, 9648–9657. [CrossRef] [PubMed]
133. Hu, J.; Qian, H.; Han, S.; Zhang, P.; Lu, Y. Light-Activated Virtual Sensor Array with Machine Learning for Non-Invasive Diagnosis of Coronary Heart Disease. *Nano-Micro Lett.* **2024**, *16*, 274. [CrossRef] [PubMed]
134. Krayden, A.; Avraham, M.; Ashkar, H.; Blank, T.; Stolyarova, S.; Nemirovsky, Y. TinyML-Based Real-Time Drift Compensation for Gas Sensors Using Spectral–Temporal Neural Networks. *Chemosensors* **2025**, *13*, 223. [CrossRef]
135. Prakasha, B.S.; Xiao, P.; Jose Esplandiu, M.; Yang, J.; Navarro-Urrios, D.; Rodriguez-Viejo, J.; Sledzinska, M. Impedance-Assisted Multivariate Analysis Technique for Enhanced Gas Sensing with 2D Dichalcogenides. *ACS Sens.* **2025**, *10*, 2712–2720. [CrossRef] [PubMed]
136. Zhou, Y.; Heng, Y.; Zhu, J.; Qian, C.; Wang, T.; Nguyen, D.H.; Jiao, M. Enhanced Gas Recognition of Electronic Nose Using 1-D Convolutional Neural Network with Savitzky–Golay Filter. *IEEE Sens. J.* **2024**, *24*, 10769–10778. [CrossRef]
137. Korotcenkov, G.; Tolstoy, V.P. Current Trends in Nanomaterials for Metal Oxide-Based Conductometric Gas Sensors: Advantages and Limitations-Part 2: Porous 2D Nanomaterials. *Nanomaterials* **2023**, *13*, 237. [CrossRef] [PubMed]
138. Wan, X.; Miao, X.; Yao, J.; Wang, S.; Shao, F.; Xiao, S.; Zhan, R.; Chen, K.; Zeng, X.; Gu, X.; et al. In Situ Ultrafast and Patterned Growth of Transition Metal Dichalcogenides from Inkjet-Printed Aqueous Precursors. *Adv. Mater.* **2021**, *33*, e2100260. [CrossRef] [PubMed]
139. Zhao, Y.; Mao, J.; Wu, Z.; Io, W.F.; Pang, S.Y.; Zhao, Y.; Hao, J. A Clean Transfer Approach to Prepare Centimetre-Scale Black Phosphorus Crystalline Multilayers on Silicon Substrates for Field-Effect Transistors. *Nat. Commun.* **2024**, *15*, 6795. [CrossRef] [PubMed]
140. Lin, X.; Tan, R.; Shen, W.; Lv, D.; Song, W. In-Vehicle Gas Sensing and Monitoring Using Electronic Noses Based on Metal Oxide Semiconductor MEMS Sensor Arrays: A Critical Review. *Chemosensors* **2026**, *14*, 16. [CrossRef]
141. Wang, J.; Cai, L.; Chen, J.; Guo, X.; Liu, Y.; Ma, Z.; Xie, Z.; Huang, H.; Chan, M.; Zhu, Y.; et al. Transferred Metal Gate to 2D Semiconductors for Sub-1 V Operation and near Ideal Subthreshold Slope. *Sci. Adv.* **2021**, *7*, eabf8744. [CrossRef] [PubMed]
142. Alzu'bi, A.; Alomar, A.; Alkhaza'leh, S.; Abuarqoub, A.; Hammoudeh, M. A Review of Privacy and Security of Edge Computing in Smart Healthcare Systems: Issues, Challenges, and Research Directions. *Tsinghua Sci. Technol.* **2024**, *29*, 1152–1180. [CrossRef]
143. Kim, S.J.; Koh, H.-J.; Ren, C.E.; Kwon, O.; Maleski, K.; Cho, S.-Y.; Anasori, B.; Kim, C.-K.; Choi, Y.-K.; Kim, J.; et al. Metallic $Ti_3C_2T_x$ MXene Gas Sensors with Ultrahigh Signal-to-Noise Ratio. *ACS Nano* **2018**, *12*, 986–993. [CrossRef] [PubMed]
144. Tian, X.; Cui, X.; Xiao, Y.; Chen, T.; Xiao, X.; Wang, Y. Pt/MoS_2/Polyaniline Nanocomposite as a Highly Effective Room Temperature Flexible Gas Sensor for Ammonia Detection. *ACS Appl. Mater. Interfaces* **2023**, *15*, 9604–9617. [CrossRef] [PubMed]
145. Chen, W.Y.; Jiang, X.; Lai, S.-N.; Peroulis, D.; Stanciu, L. Nanohybrids of a MXene and Transition Metal Dichalcogenide for Selective Detection of Volatile Organic Compounds. *Nat. Commun.* **2020**, *11*, 1302. [CrossRef] [PubMed]